A critical review on bismuth and antimony halide based perovskites and their derivatives for photovoltaic applications: Recent advances and challenges

ARTICLE

A critical review on Bismuth and Antimony- based halide perovskites and their derivatives for photovoltaic applications: recent advances and challenges

Received 00th January 20xx,
Accepted 00th January 20xx

DOI: 10.1039/x0xx00000x

Zhixin Jin,[ab] Zheng Zhang,[b] Jingwei Xiu,[b] Haisheng Song,*[a] Teresa Gatti,[c]* and Zhubing He[b]*

Since more than 10 years, lead halide perovskites play the key role of light-absorbers in next-generation low-cost and high-efficiency thin film solar cells. Due to their superior and unique photovoltaic properties, such as the high absorption coefficient, the long diffusion length of excitons and lifetime of photogenerated charge carriers, the power conversion efficiency of solar cell based on these materials has overcome the 25% threshold, thus competing with traditional silicon-based photovoltaics. However, the toxicity and low environmental stability of the lead-based photo-active species they contain strongly limit their commercialization. Within this scenario, research investigations directed at assessing properties and opportunities offered by emerging lead-free halide perovskites are becoming everyday more relevant to pinpoint new low-cost/low-toxicity solutions for solar-to-electricity conversion. In this review, group VA, namely Bismuth (Bi) and Antimony (Sb), based halide perovskites and their derivative materials with different valence states are classified based on formulas of $A_3B_2X_9$, A_2AgBX_6, also known as double perovskites, and $Ag_aBi_bX_{a+3b}$, called Rudorffites (A = MA, Cs, Rb, etc.; B = Bi, Sb; X = I, Br, Cl). Here, we summarize the recent progresses in exploitation of these materials, with a special attention devoted to the description of the crystal structures, the thin film preparation methods and the performances in real device, including both theoretical insights and experimental observations. With this survey, we are able to provide reasonable perspectives for the future development of high-performance lead-free bismuth/antimony based halide based perovskite and their derivative solar cells.

Formattato: Evidenziato

1. Introduction

Organic-inorganic hybrid lead halide perovskite solar cells (PvSCs) have attracted huge attention in the last decade as one of the most promising low-cost technologies with power conversion efficiency (PCE) overcoming the 25% threshold.[1] The mostly investigated metal halide perovskites have formula $APbX_3$, where A is a monovalent cation, e.g., methylammonium ($CH_3NH_3^+$, MA^+), formamidinium ($HC(NH_2)_2$, FA^+), Cs^+ and X is a halide anion such as I^-, Br^-, Cl^-. The $APbX_3$ perovskite is an excellent photo-active material for photovoltaics due to the unique optoelectronic properties, including the direct and suitably narrow band gap,[2] the extremely high absorption coefficient,[3] the long charge carrier diffusion length,[4] the high defect tolerance,[5] the excellent ambipolar charge carrier transport properties[6] and the possibility to undergo solution-processing at low temperature.[7]

Lead-based PvSCs have been largely developed due to the above summarized advantages. However, two main bottlenecks, that hinder future industrialization

[a] Wuhan National Laboratory for Optoelectronics, Huazhong University of Science and Technology, Luoyu Road 1037, Wuhan 430074, P.R. China.
[b] Department of Materials Science and Engineering, Shenzhen Key Laboratory of Full Spectral Solar Electricity Generation (FSSEG), Southern University of Science and Technology, No. 1088, Xueyuan Rd., Shenzhen 518055, Guangdong, China.
[c] Center for Materials Research, Justus Liebig University, Heinrich Buff Ring 17, 35392, Giessen, Germany.

and commercialization of these solar technologies, are found in the poor stability towards environmental factors (humidity, heat, UV-radiation etc.) and the high toxicity of lead. These disadvantages of Pb-based perovskites prompted many researchers to seek alternatives based on more stable and environmentally friendly elements. Lead-free halide perovskite-based light absorbers mainly include post-transition metal or metalloid elements like Sn,[8] Ge,[9] Sb,[10] Bi,[11,12] and others.[13] The Sn and Ge elements belong to the same group of Pb in periodical table, but Sn^{2+} and Ge^{2+} can be easily oxidized into Sn^{4+} and Ge^{4+}, resulting in the rapid degradation of the corresponding perovskite's photovoltaic properties. In addition, tin compounds are also toxic and their effects on the environment and on humans are well known and documented. On the other hand, group VA post-transition metals like Bi and Sb, also largely available from natural sources, are characterized by a high chemical stability in their trivalent form and by a lower toxicity compared to Pb^{2+} and Sn^{2+}. These ions have similar electronic configuration, electronegativity, and ionic radius to Pb^{2+}. Capitalizing on the excellent stability and low-toxicity, research on Bi and Sb-based perovskite and their derivatives solar cells have emerged as a new, largely explored sector. Nowadays, the excellent level of maturity for them allows us to make insightful considerations from data analysis.

Indeed, in recent years, group VA-based ~~perovskite and their derivative~~ solar cells have been greatly developed, and many material combinations have been identified as emerging light absorbers, such as $MA_3Bi_2I_9$, $Cs_3Bi_2I_9$, $MA_3Sb_2I_9$, $Cs_3Sb_2I_9$ and more. However, relatively wide bandgaps, high exciton binding energies and heavy carrier effective masses ultimately limit their photovoltaic performance. Currently, the PCE of VA-based perovskite and their derivatives solar cells lay far behind that of Pb-based PvSCs.

In this review, we provide a summary of the recent developments on VA metal- based halide perovskites and their derivatives, mainly focusing on the $A_3B_2X_9$, double perovskite and Rudorffite structures. We further discuss the potential applications of these emerging species in photovoltaics with emphasis on theoretical and physico-chemical studies, thin films fabrication strategies, carrier extraction layers screening and device structure optimization. Accordingly, we also provide critical hints on future challenges for these materials to become protagonists in research on next-generation, ultra-cheap photovoltaics.

2. Structures and properties of group VA halides perovskites and their derivatives

As adjacent elements of Pb, the VA group metals (Bi and Sb) have been employed for the replacement of lead in classical hybrid and all-inorganic halide perovskite-based photon absorbers. Since Bi and Sb have three valence electrons in the outer shell and thus provide trivalent cations, when used to replace Pb^{2+}, structures with different dimensionality can be formed in relation to the types of connection in BiX_6^{3-} (and SbX_6^{3-}) octahedron, in order to ensure the stability of the crystalline lattice. In this section, a brief introduction of typical $A_3B_2X_9$ (A = MA^+, FA^+, Cs^+ etc.; B = Bi^{3+}, Sb^{3+}; X = I^-, Br^-, Cl^-) polymorphs and other perovskite derivatives will be analyzed. The multiple connection modes of BX_6^{3-} lead to a large dimensional variability in crystal structures of group VA- based perovskites and their derivative ~~material~~s. Generally, the $A_3B_2X_9$ is commonly adopted in bismuth halides based or antimony halides based hybrids, along with zero dimensional (0D) or two dimensional (2D) structures. In addition, the double perovskite structures, with a general formula of $A_2B^IB^{III}X_6$, maintain a three dimensional (3D) corner-sharing perovskite structures with monovalent metals (B^I) and trivalent metals (B^{III} = Bi, Sb). Another family of photovoltaic perovskite derivatives of formula $A_aB_bX_{a+3b}$ (A = Ag^+, Cu^+, etc.; B = Bi^{3+}, Sb^{3+}; X = I^-, Br^-, Cl^-) can also be formed as Rudorffite structures which have 3D structures based on edge-shared $[AX_6]$ and $[BX_6]$ octahedral. Here we denote them as 0D, 2D, double perovskite (3D) and Rudorffite structures (3D) (Fig. 1).

Formattato: Evidenziato

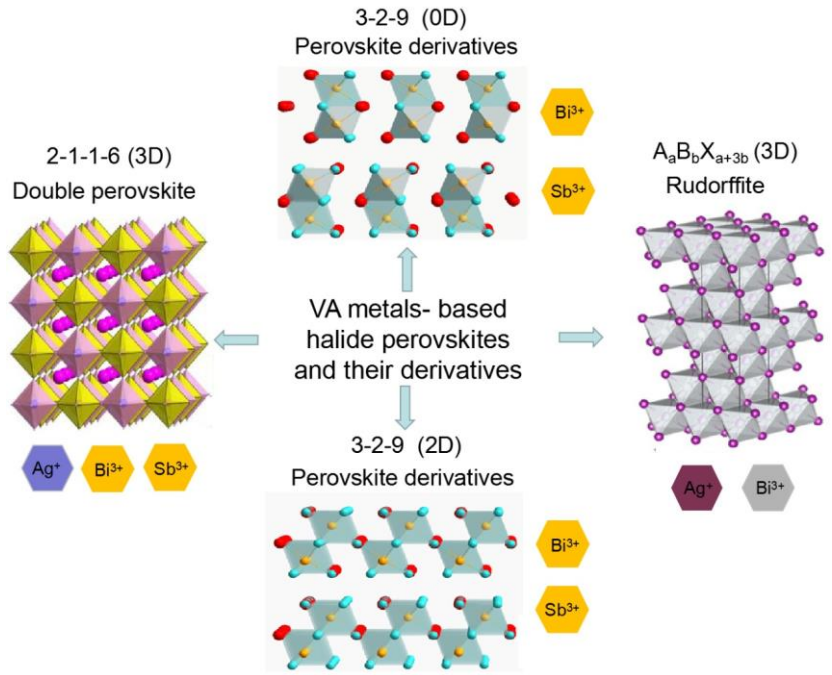

Fig. 1 Crystal structures of group VA- based halide perovskites and their derivatives. Reproduced with permission.[28] Copyright 2017, Wiley-VCH. Reproduced with permission.[101] Copyright 2019, Elsevier. Reproduced with permission.[106] Copyright 2019, Wiley-VCH.

2.1 Bismuth based halide perovskites and their derivatives

From the point of the electronic structure, the excellent properties of lead-based perovskites are mainly due to the $6s^26p^0$ electronic configuration of Pb^{2+}, which allows the hybridization of the iodide 5p orbitals in the valence band with the 6p orbitals of lead in the conduction bands. The large absorption coefficient is mainly derived from the high density of states which are produced by the p-orbital-based interatomic transition and s-p-orbital-based intra-atomic transition. The existence of shallow defect states relies on the strong antibonding coupling between the 6s orbital of lead and 5p orbital of iodide in the valence band.[14,15] Fortunately, Bi^{3+} and Pb^{2+} have very similar ionic radii, and also have the same $6s^26p^0$ electronic configuration, which may make it easy for Bi to replace Pb in the perovskite lattice. Hence, Bi^{3+} is a good potential candidate for lead substitution.

Bismuth halides based perovskite derivatives $A_3Bi_2I_9$ (A = K, Rb, and Cs) have been prepared and used for photovoltaic applications.[16] The compounds can have two types of structure, namely 0D and 2D. $Cs_3Bi_2I_9$ crystallizes in the space group $P6_3/mmc$ with a 0D hexagonal close packing structure containing isolated $Bi_2I_9^{3-}$ cluster dimeric units comprising pairs of face-sharing Bi-I octahedra (Fig. 2a). The reduced dimensionality of 0D $A_3Bi_2X_9$ systems with respect to 3D $ABiX_3$ materials can deliver better stability against phase degradation. On the other hand, compounds like $K_3Bi_2I_9$ and $Rb_3Bi_2I_9$ have 2D structures with corrugated layers based on corners connected Bi-I octahedron (Fig. 2b). More importantly, lattice parameters in $A_3B_2X_9$ perovskite derivatives can be tuned by A, B, X site substitutions. The band gaps can vary from 1.9 to 3.1 eV.[17] By computing dielectric properties, anomalously

large Born effective charge tensors on Bi^{3+} are found due to the proximal structure instabilities of the Bi^{3+} $6s^2$ lone pair. The defect screening and the effective charge carrier transport are improved by these Born effective charges. The band positions of $A_3Bi_2I_9$ are shown in Fig. 2c, as obtained by combining density functional theory (DFT) calculations and experimental values.

$MA_3Bi_2I_9$ is the most studied polymorph among all the bismuth halides based absorbers. The structure of $MA_3Bi_2I_9$ comprising two face-sharing bismuth iodide octahedra, is a 0D dimer at room temperature. In contrast to $MAPbX_3$, pure phase $MA_3Bi_2I_9$ has been synthesized by solution and vapor methods and it is air stable. $MA_3Bi_2I_9$ has an indirect bandgap of 2.04 eV, with optical absorption coefficients approaching 10^5 cm^{-1}. A long photoluminescence (PL) decay of at least 760 ps, with a bulk lifetime possibly close to 5.6 ns, was measured by Hoye et al.[18] Sulfur-doped $MA_3Bi_2I_9$ have been obtained by *in situ* sulfur doping *via* the thermal decomposition of a $Bi(xt)_3$ (xt = ethyl xanthate) precursor. Compared to $MA_3Bi_2I_9$, the sulfur-doped bismuth perovskite derivatives exhibited a smaller bandgap of 1.45 eV. Colors of the obtained films clearly changed from orange to black when annealed from 80 to 150 ºC (Fig. 2d). Sulfur-doped $MA_3Bi_2I_9$ exhibited a much higher carrier mobility and carrier concentration than pristine $MA_3Bi_2I_9$.[19]

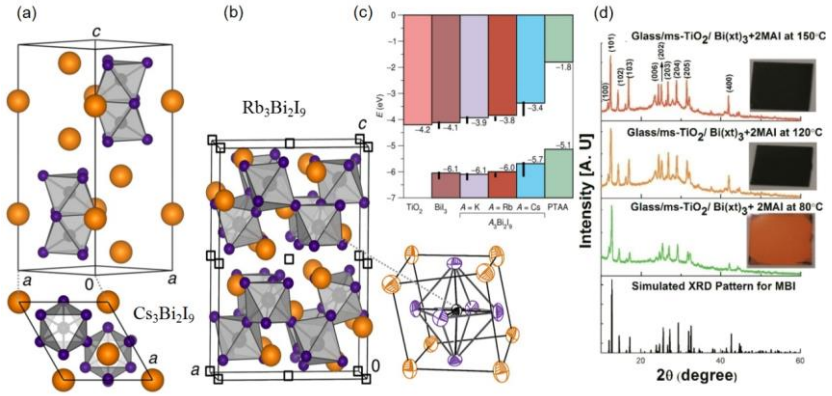

Fig. 2 Crystal structures of (a) $Cs_3Bi_2I_9$ and (b) $Rb_3Bi_2I_9$ with details of a single octahedron. (c) Trends in band gaps of compounds $A_3Bi_2I_9$ (A is an alkali metal). Reproduced with permission.[16] Copyright 2015, American Chemical Society. (d) XRD patterns and color variations for sulfur-doped $MA_3Bi_2I_9$ at different temperatures. Reproduced with permission.[19] Copyright 2016, American Chemical Society.

Other organic groups replacing MA^+ have also been employed. $MA_3Bi_2Cl_9$ is a one dimensional (1D) organic-inorganic hybrid bismuth compound with double chains of distorted $BiCl_6^{3-}$ octahedra structure.[20] 1D thermally stable $(H_3NC_6H_{12}NH_3)BiI_5$ was synthesized as photoactive layer including organic 1,6-hexanediammonium groups. Compared to $MAPbI_3$, $(H_3NC_6H_{12}NH_3)BiI_5$ exhibited better thermal stability.[21] A new organic-inorganic compound of formula $C_6H_{14}NBi_2I_9$ exhibiting a 0D structure has been synthesized by solvent evaporation. Thin films have also been prepared by spin coating.[22] $C_5H_6NBiI_4$ ([py][BiI_4])(py: pyridinium) and $C_6H_8NBiI_4$ ([mepy][BiI_4])(mepy: 1-methylpyridnium) have been prepared containing 1D BiI^{4-} anionic chains built by edge-sharing BiI_6.[23] Dark-red $(NH_4)_3Bi_2I_9$ was synthesized through a solution method and featured a 2D layered ~~perovskite derivatives~~ structure, with a measured band gap of 2.04 eV.[24]

Bismuth based 3D double perovskites were also developed, as the 3D lead-based ones show the best optoelectronic performances. A 3D double perovskite

with the chemical formula of $A_2B^IB^{III}X_6$ has been produced by incorporating a monovalent metal into Bi^{3+} site. The total charge neutrality is maintained thanks to the presence of monovalent and trivalent cations occupying the B^I and B^{III} sites (Fig. 3a). Giorgi and Yamashita theoretically investigated double perovskites of the type MA_2TlBiI_6, where Pb^{2+} cations in $MAPbI_3$ are substituted by the Tl^+/Bi^{3+} ionic pairs.[25] Although it is predicted to have good photoelectric potential, monovalent Tl is highly toxic and therefore it is not suitable for practical applications. The double perovskite structure that currently attracts the largest attention is Cs_2AgBiX_6. $Cs_2AgBiBr_6$ is characterized by a long room-temperature PL lifetime of more than 600 ns and has an indirect bandgap of around 1.95 eV. This compound is characterized by a better stability to heat and moisture compared to $MAPbI_3$.[26] McClure et al. reported on the double perovskites $Cs_2AgBiBr_6$ and $Cs_2AgBiCl_6$ synthesized from both solid state and solution routes.[27] They found indirect band gaps of 2.19 eV and 2.77 eV, respectively, by diffuse reflectance measurements and band structure calculations. When exposed to air these compounds are stable, but when exposed to both air and light for more than a week, $Cs_2AgBiBr_6$ starts to degrade. Finally, another family of photovoltaic halides based on two aliovalent metals is the one with general formula $Ag_aBi_bI_x$ (x=a+3b), based on edge-shared AX_6 and BX_6 octahedra. This structure is called Rudorffite and has a 3D *R3m* trigonal lattice (Fig. 1). Several Ag-Bi-I Rudorffites structures have direct band gaps in the range of 1.79-1.83 eV and feature highly stability in air.[28]

2.2 Antimony based halide perovskites and their~~perovskite~~ derivatives

Being also member of group VA, antimony, a metalloid, is also expected to exhibit optoelectronic behavior similar to Bi when integrated into halide perovskite-type or derivedatives structures. Sb^{3+} ions have similar structure to Bi^{3+} and ternary halide semiconductors such as $Cs_3Sb_2I_9$ have been examined by computational and experimental approaches. The 0D dimeric form (space group $P6_3/mmc$) and the 2D layered form ($P\,3\,m1$) are two structural modifications in $Cs_3Sb_2I_9$.

To achieve correct charge balance, the hypothetical perovskite compound $CsSbI_3$ may produce the crystal structure of the 2D layered $Cs_3Sb_2I_9$ after removal of one layer in every third Sb layer along the <111> direction (Fig. 3b).[10] 2D $Cs_3Sb_2I_9$ has an optical band gap of 2.05 eV and an enhanced stability under ambient air compared to $MAPbI_3$. Cs can be replaced by other alkali metals such as Rb and K, providing compounds with general formula $A_3Sb_2X_9$. Experiments have proven that the A-site cation plays an important role in determining the structural and optoelectronic properties of these compounds. $Rb_3Sb_2I_9$ and $K_3Sb_2I_9$ have a direct bandgap and 2D structures due to the smaller ionic radius of Rb^+ and K^+ compared to Cs^+, which stabilizes this type of structure.[29] In addition, colloidal $Cs_3Sb_2I_9$ and $Rb_3Sb_2I_9$ nanocrystals have been synthesized.[30] They also exhibit 2D crystal structures and a high absorption cross-section of 10^{15} cm^2, standing out as good candidates for optoelectronic applications.

The hexagonal structure of methylammonium antimony iodide ($MA_3Sb_2I_9$) is isomorphous with $Cs_3Sb_2I_9$ at room temperature.[31] Hebig et al. reported a $MA_3Sb_2I_9$ compound produced through a solution-based method. By photothermal deflection spectroscopy (PDS), amorphous $MA_3Sb_2I_9$ results to have an absorption coefficient $\alpha \approx 10^5$ cm^{-1} and an optical band gap of 2.14 eV, with a pretty large energetic disorder, as evidenced by an Urbach tail (E_u) of 62 meV and a weak PL emission shifted at 1.58 eV, likely originated from radiative recombination involving sub-gap states.[32] So far, most synthesized antimony–based halide double perovskites appear to have large bandgaps (> 2 eV). Recently, powders of $Cs_2SbAgCl_6$ and Cu^{2+}-doped $Cs_2SbAgCl_6$ were investigated. Cu^{2+}-doped $Cs_2SbAgCl_6$ has a reduced indirect bandgap of 1.02 eV compared to the 2.65 eV found for $Cs_2SbAgCl_6$.[33] On the other hand, the layered double perovskite $Cs_{3+n}M(II)_nSb_2X_{9+3n}$, where $[SnI_6]$ and $[GeI_6]$ octahedral layers are introduced between $[Sb_2I_9]$ clusters, providing an increased electronic dimensionality (Fig. 3c), reaches smaller band gaps, smaller carrier effective masses, larger dielectric constants, lower exciton binding energies and higher optical absorption compared to $Cs_3Sb_2I_9$.[34] Vargas et al. have reported that the band gap of $Cs_4Mn_{1-x}Cu_xSb_2Cl_{12}$ (x = 0−1) can be modulated from 3.0 to 1.0 eV by adjusting the ratio of manganese to copper in the mixed chlorides,[35] as shown in Fig. 3d.

Formattato: Evidenziato

Meanwhile, the magnetic properties of these halide perovskites and their derivatives can be also systematically tuned through such a compositional engineering process.

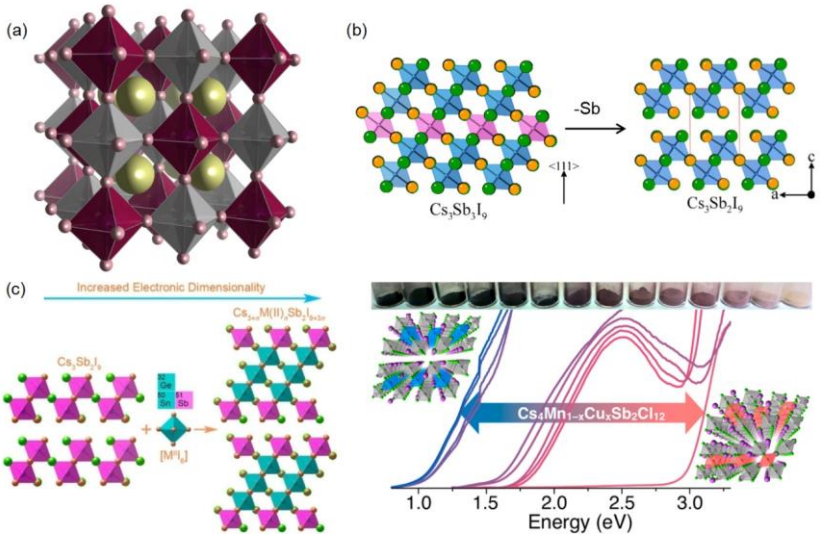

Fig. 3 (a) The structure of a model double perovskite. Reproduced with permission.[39] Copyright 2016, American Chemical Society. (b) The modification of the structure of 2D layered $Cs_3Sb_2I_9$ following removal of one Sb-layer every 3 along the <111> direction. Reproduced with permission.[10] Copyright 2015, American Chemical Society. (c) Schematic representation of the crystal structure of M^{2+}-doped $Cs_3Sb_2I_9$. Reproduced with permission.[34] Copyright 2018, American Chemical Society. (d) The change in band gap after compositional engineering of $Cs_{3+n}M(II)_nSb_2X_{9+3n}$. Reproduced with permission.[35] Copyright 2018, American Chemical Society.

3. Theoretical studies on group VA halide perovskites and their derivatives

Bismuth–based halide perovskites and perovskite derivatives solar cells have been simulated using the General-Purpose Photovoltaic Device Model (GPVDM). The results display a bismuth halides based device characterized by a 20% PCE at an active layer thickness of 450 nm.[36] At the same time, a series of theoretical simulations on group VA-based perovskites and their derivatives were carried out. First principles DFT calculation can simulate the electronic structures of many body systems from atomic level quantum mechanics. For example, the electronic structures of various perovskites were simulated by first principles calculations, providing good information on their band gaps, defects distributions, charge carriers mobilities, absorption spectra and more.[37,38]

By theoretical simulation, all the elements of the periodic table which can be integrated into double perovskites with general formula $A_2BB^{3+}X_6$ are showed in Fig. 4a. The A^+, B^+, B^{3+}, X^- sites can be occupied by 7, 8, 34, 5 elements, respectively. These elements can yield nearly 10000 compounds. However, following Goldschmidt's rules on perovskite structure stability, the majority of these compounds are unstable. By the most rigorous screening criteria, there are more than 600 compounds whose synthesis could be attempted.[39] The double perovskites based on Bi or Sb have been

analyzed through the first-principle calculations and experimentally.[40] Their electronic band structure and effective masses have been calculated using the PBE0 hybrid functional and DFT/LDA (local density approximation), respectively (Fig. 4b). Most double perovskites were predicted to display an indirect gap from calculations, unless some new experimental strategies were developed for changing them into direct-gap. For example, the synthesized $Cs_2AgBiCl_6$ compound is a face-centered cubic double perovskite with an indirect gap of 2.2 eV. In general, the eleven optimal double perovskite materials have been screened by first-principles calculations exploiting the strategy of cation-transmutation and are characterized by an intrinsic thermodynamic stability, relatively small band gaps and light carrier effective masses. Among them, $Cs_2InSbCl_6$ and $Cs_2InBiCl_6$, two materials with a 1.0 eV direct band-gap, show the greatest potential as photovoltaic materials (Fig. 4c).[41] However, perspectives for perovskites based on low-toxicity bismuth ions might expand well-beyond the Cs_2AgBiX_6 motif, as predicted by first principle calculations. [42]

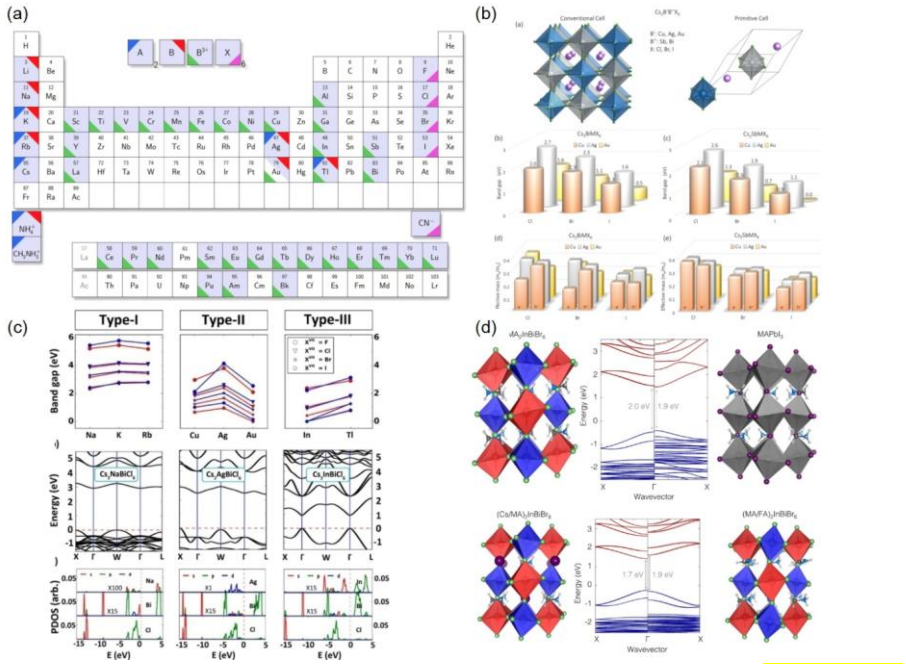

Fig. 4 (a) Elements that can constitute halide double perovskites with general composition $A_2BB^{3+}X_6$. Reproduced with permission.[39] Copyright 2016, American Chemical Society. (b) Calculated band gaps and effective hole/electron masses for Cs_2BiMX_6 and Cs_2SbMX_6 (M = Cu, Ag or Au, X = Cl, Br or I). Reproduced with permission.[40] Copyright 2016, American Chemical Society. (c) Variation of band gaps, electronic band structures and orbital projected density of states of typical materials in the categories: $Cs_2NaBiCl_6$, $Cs_2AgBiCl_6$, $Cs_2InBiCl_6$. Reproduced with permission.[41] Copyright 2017, American Chemical Society. (d) Electronic and optical properties of hypothetical halide double perovskites of formulas $MA_2InBiBr_6$, $(Cs/MA)_2InBiBr_6$, and $(MA/FA)_2InBiBr_6$. Reproduced with permission.[48] Copyright 2017, American Chemical Society.

Compounds like $MABiSeI_2$ and $MABiSI_2$ could be prepared by introducing two anions for preserving the charge neutrality from the split-anion approach.[43,44] These species might be characterized by a direct band gap of 1.3 to 1.4 eV, ideal for single-junction solar cells (Fig. 5).[45] Other theoretical calculations on possible double perovskite structures have also been carried out.[46,47] Volonakis et al. theoretically investigated

Cs_2InBiX_6 and the mixed-cation $(Cs/MA/FA)_2InBiBr_6$ halide double perovskites. $A_2InBiBr_6$ could be stabilized by employing of MA and FA as the A cations. The calculated band gaps with DFT/PBE0 of $MAPbI_3$ and $MA_2InBiBr_6$ are 1.9 eV and 2.0 eV, respectively. Band gaps of 1.7 eV and 1.9 eV are calculated for mixed A cation species such as $[(Cs_{0.5}MA_{0.5})_2InBiBr_6]$ or $[(FA_{0.5}MA_{0.5})_2InBiBr_6]$, respectively (Fig. 4d). This suggests that a certain tuning of band gaps is possible within a limited range for mixed cation double perovskites.[48] Yang et al. found that the band gap of $Cs_2AgBiBr_6$ can be changed systematically by modifying lattice parameters. The band gap of ordered $Cs_2AgBiBr_6$ is an indirect one of 1.93 eV and could be modified into a pseudo-direct disordered one of 0.44 eV through a tight control on doping and growth temperature.[49] The difference between the pseudo-closed s^2 orbitals of Tl and In could lead to different semiconducting behavior Tl-Bi and In-Bi bromide double perovskites, as evidenced by DFT calculations. Tl-Bi double perovskites show p-type semiconducting properties, while In-Bi ones are p-type metallic ones. Therefore, this analysis emerges that In-Bi bromide double perovskites should be disregarded as light absorbers, but could be perhaps suitable as hole-transport layer (HTL) in PvSCs.[50]

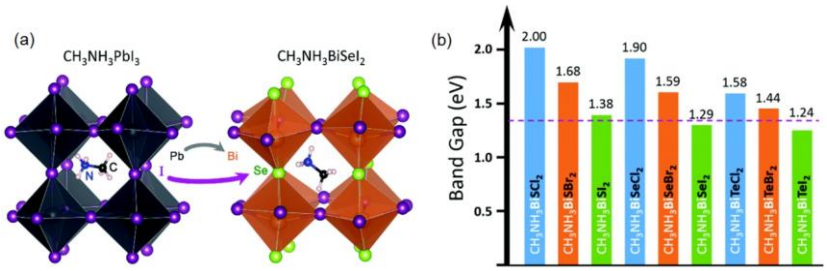

Fig. 5 (a) Details on crystal structures of $MABiSeI_2$ and $MAPbI_3$. (b) HSE (Heyd-Scuseria-Ernaerhof)-SOC (spin-orbit coupling) calculated band gaps of $MABiXY_2$ where X is Te, Se or S and Y is I, Br or Cl. The dashed line marks the optimal band gap of a single-junction solar cell according to the Shockley-Queisser theory. Reproduced with permission.[45] Copyright 2016, the Royal Society of Chemistry.

Deng et al. synthesized double perovskites $Cs_2AgSbCl_6$ via a solution-based method. The compound has a computed indirect bandgap of 2.41 eV by projected augmented wave (PAW) + HSE06 hybrid functional calculations. The result is comparable with the experimental value of 2.60 eV. In addition, $Cs_2AgSbCl_6/TiO_2$ heterostructures show an improved light absorption compared to the pure perovskite and a decreased interface bandgap due to the formation of interfacial states.[51] The structures and electronic properties of Sb_2S_3, $Cs_2Sb_8S_{13}$, $MA_2Sb_8S_{13}$ have been investigated by first-principles techniques. Their electronic band structures are predicted through DFT/HSE06 to have band gaps of 1.72, 1.85 and 2.08 eV, respectively. Remarkably, the introduction of the A cations in the pristine Sb_2S_3 to yield $Cs_2Sb_8S_{13}$ and $MA_2Sb_8S_{13}$ leads to a significant decrease in the band gaps depending on that specific A cation, thus it allows to obtain good performances for solar harvesting applications.[52]

4. Group VA based halide perovskites and their derivatives for photovoltaics

Due to their unique optoelectronic properties and structural stabilities, the low-toxicity Bi and Sb based halide perovskites and their derivates are considered promising absorbers to substitute lead-based compounds in PvSCs and have done enormous progresses in recent years in terms of improved power conversion efficiencies (PCE). In the following part of this review, we will provide a detailed summary of the main examples presented in the recent literatures on the use of these compounds in photovoltaic devices.

4.1 Bismuth based halide perovskite and their derivatives solar cells

4.1.1 Photovoltaic devices based on perovskite derivatives

The recorded device performances of bismuth based halide perovskite derivatives solar cells (PvDSCs) are summarized in Table 1. Park et al. first reported bismuth halides based perovskites derivatives of formula $A_3Bi_2I_9$ used as light absorbers in solar cells.[11] The preparation of $Cs_3Bi_2I_9$, $MA_3Bi_2I_9$, and $MA_3Bi_2I_9Cl_x$ was carried out through a simple one-step spin coating method. The light absorption spectra and band gaps for the three different materials were listed for comparison, as shown in Fig. 6a. Among them, the $Cs_3Bi_2I_9$ perovskite derivative shows the highest absorption coefficient and the lowest structural disorder (lowest E_u value) and this is consequence of the different morphologies that the materials assume in thin film form. Doping with chlorides further changes the morphology of the film from an interconnected and smooth layer to a nanostructured one. Comparison of photovoltaic data indicates that the best device is the one based on $Cs_3Bi_2I_9$, with a short circuit current density (J_{sc}) of 2.15 mA cm^{-2}, an open circuit voltage (V_{oc}) of 0.85 V, a fill factor (FF) of 0.60 and an overall PCE of 1.09% in a mesoscopic solar cell architecture. By contrast, $MA_3Bi_2I_9$ device provides J_{sc} = 0.52 mA cm^{-2}, V_{oc}= 0.68 V, FF = 0.33, and PCE = 0.12%, while $MA_3Bi_2I_{9-x}Cl_x$ one provides very poor figure of merit (PCE =0.003%). Photocurrent density-voltage (*J-V*) curves of these devices are shown in Fig. 6b. The author points out that the sub-optimal morphology, constituted of perovskite derivative particles surrounded by amorphous $BiCl_3$ is the major cause of the extremely low efficiency found for $MA_3Bi_2I_{9-x}Cl_x$. At the same time, the first inverted planar heterojunction device based on $MA_3Bi_2I_9$ was reported. The band gap of $MA_3Bi_2I_9$ is relatively high, 2.9 eV, and therefore PCE for this device is very low, about 0.1% (Fig. 6c).[53]

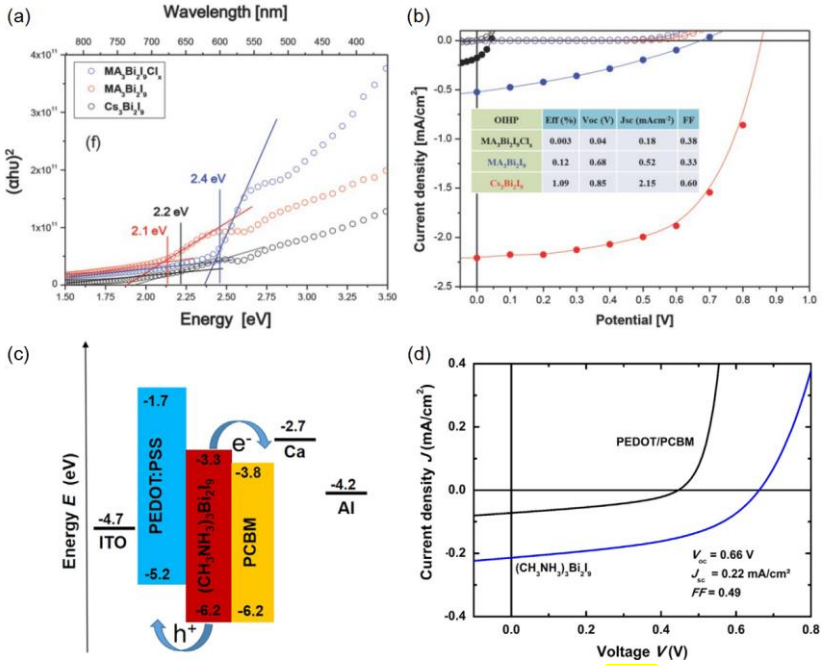

Fig. 6 (a) Tauc plots for $MA_3Bi_2I_9Cl_x$, $MA_3Bi_2I_9$, $Cs_3Bi_2I_9$ thin films. (b) *J-V* curves for PvDSC based on the three different materials as in (a) as light absorbers. Reproduced with permission.[11] Copyright 2015, Wiley VCH. (c) Energy level diagram and

(d) *J-V* curves under illumination for planar heterojunction devices based on the $MA_3Bi_2I_9$ absorber. Reproduced with permission.[53] Copyright 2016, Elsevier.

Lyu et al. first demonstrated that Bi^{3+} may replace lead/tin in solution processed PvSC. Using poly(3-hexylthiophene-2.5-diyl) (P3HT) to replace spiro-OMeTAD as the HTL in a PvDSC, they demonstrated a PCE of 0.19% employing $MA_3Bi_2I_9$ in substitution of $MAPbI_3$.[54] The morphology and crystallinity of the solution-processed $MA_3Bi_2I_9$ film and photovoltaic properties of the resulting solar devices can be affected by the precursor solution concentration and substrate used for deposition. The efficiency of the PvDSC was further improved to 0.42% on a mesoporous TiO_2 electron transporting layer (ETL) scaffold.[55] The $MA_3Bi_2I_9$ devices were found to be very stable in ambient air, maintaining a stable 0.2% PCE for more than 10 weeks.[56] Further studies indicate that the PCE of PvDSC based on the non-toxic $MA_3Bi_2I_9$ can be further increased by improving thin film quality and by proper engineering of the device structure.[57]

Table 1 Summary of device performances for bismuth based halide PvDSCs

Device structure	E_g (eV)	J_{sc} (mA/cm^2)	V_{oc} (V)	FF	PCE (%)	Ref.
FTO/TiO_2/meso-TiO_2/$MA_3Bi_2I_9$/Spiro-OMeTAD/Ag	2.10	0.52	0.68	0.33	0.12	[11]
FTO/TiO_2/meso-TiO_2/$Cs_3Bi_2I_9$/Spiro-OMeTAD/Ag	2.20	2.15	0.85	0.60	1.09	[11]
FTO/TiO_2/meso-TiO_2/$(H_3NC_6H_{12}NH_3)Bi_5$/Spiro-OMeTAD/Au	2.10	0.115	0.40	0.43	0.027	[21]
FTO/TiO_2/ZrO_2/$C_5H_6NBiI_4$/Carbon	1.78	2.71	0.62	0.54	0.9	[23]
ITO/PEDOT:PSS/$MA_3Bi_2I_9$/PCBM/Ca/Al	2.90	0.22	0.66	0.49	0.1	[53]
FTO/TiO_2/meso-TiO_2/$MA_3Bi_2I_9$/P3HT/Au	2.10	1.157	0.35	0.464	0.19	[54]
FTO/TiO_2/meso-TiO_2/$MA_3Bi_2I_9$/Spiro-OMeTAD/MoO_3/Ag	2.10	1.00	0.67	0.625	0.42	[55]
FTO/TiO_2/meso-TiO_2/$MA_3Bi_2I_9$/Spiro-OMeTAD/Au	-	0.83	0.56	0.49	0.26	[56]
FTO/TiO_2/$MA_3Bi_2I_9$/Spiro-OMeTAD/Au	2.10	0.49	0.72	0.32	0.11	[57]
FTO/TiO_2/meso-TiO_2/$MA_3Bi_2I_9$/Spiro-OMeTAD/Au	2.26	2.95	0.81	0.69	1.64	[59]
FTO/TiO_2/meso-TiO_2/$MA_3Bi_2I_9$/P3HT/Au	2.20	4.02	1.01	0.78	3.17	[60]
ITO/PEDOT:PSS/$MA_3Bi_2I_9$/C60/BCP/Ag	2.22	1.39	0.83	0.34	0.39	[61]
FTO/TiO_2/meso-TiO_2/$MA_3Bi_2I_9$/Spiro-OMeTAD/Au	-	0.94	0.51	0.61	0.31	[62]
FTO/TiO_2/meso-TiO_2/$MA_3Bi_2I_9$/Spiro-OMeTAD/Au	2.10	1.10	0.65	0.50	0.36	[63]
FTO/TiO_2/meso-TiO_2/$MA_3Bi_2I_9$/PIF8-TAA/Au	2.10	1.15	0.85	0.73	0.71	[65]
FTO/TiO_2/meso-TiO_2/$MA_3Bi_2I_9$/Spiro-OMeTAD/Au	2.10	0.17	0.84	0.35	0.05	[66]
FTO/TiO_2/$MA_3Bi_2I_9$/Spiro-OMeTAD/Ag	2.10	0.37	0.69	0.32	0.08	[67]
FTO/FPDI/$MA_3Bi_2I_9$/Spiro-OMeTAD/Ag	2.10	0.37	0.61	0.28	0.06	[68]
FTO/TiO_2/meso-TiO_2/$MA_3Bi_2I_9$/PTAA/Ag	2.10	0.27	0.57	0.50	0.08	[69]
FTO/TiO_2/$MA_3Bi_2I_9$/Spiro-OMeTAD/Au	2.20	1.12	0.61	0.43	0.29	[70]
FTO/TiO_2/TiO_2 NR/$MA_3Bi_2I_9$/Spiro-OMeTAD/Au	2.10	0.69	0.59	0.37	0.15	[71]
FTO/TiO_2/meso-TiO_2/$MA_3Bi_2I_9$/Spiro-OMeTAD/Au	2.24	1.18	0.59	0.42	0.33	[72]
FTO/TiO_2/meso-TiO_2/$MA_3Bi_2I_9$/PTAA/Ag	2.08	1.07	0.59	0.42	0.26	[81]
FTO/TiO_2/meso-TiO_2/$Cs_3Bi_2I_9$/P3HT/Ag	2.30	5.78	0.86	0.64	3.20	[73]

FTO/TiO_2/meso-TiO_2/$CsBi_3I_{10}$/P3HT/Ag	1.77	3.40	0.31	0.30	0.40	[74]
FTO/TiO_2/meso-TiO_2/$Cs_3Bi_2I_9$/P3HT/Ag	2.03	0.18	0.02	0.37	0.02	[74]
FTO/TiO_2/meso-TiO_2/$CsBi_3I_{10}$/TQ1/Ag	1.77	2.38	0.62	0.52	0.77	[75]
ITO/PEDOT:PSS/$Cs_3Bi_2I_9$/PCBM/AZO/Ag	2.08	3.42	0.74	0.51	1.26	[76]
FTO/TiO_2/meso-TiO_2/$MA_3Bi_2I_{5.22}Cl_{3.78}$/PTAA/Ag	2.25	0.68	0.46	0.60	0.18	[81]
FTO/TiO_2/meso-TiO_2/$MA_3BiI_3Cl_6$/Spiro-OMeTAD/ Au	-	0.67	0.22	0.33	0.47	[82]
FTO/TiO_2/meso-TiO_2/$MA_3Bi_2I_{9-2x}S_x$/Spiro-OMeTAD/Au	1.67	0.58	0.54	0.48	0.15	[83]
ITO/NiO_x/$Cs_3Bi_2I_6Br_3$/PCBM/C_{60}/BCP/Ag	2.03	3.15	0.64	0.57	1.15	[84]

Note: Mesoporous TiO_2 is abbreviated as meso-TiO_2. TiO_2 nanorod is abbreviated as TiO_2 NR. 2,2',7,7'-Tetrakis[N,N-di(4-methoxyphenyl)amino]-9,9'-spirobifluorene is abbreviated as Spiro-OMeTAD. [6,6]-Phenyl C_{61} butyric acid methyl ester is abbreviated as PCBM. 2,9-Dimethyl-4,7-diphenyl-1,10-phenanthroline is abbreviated as BCP. Poly[bis(4-phenyl)(2,4,6-triMethylphenyl)aMine] is abbreviated as PTAA. C60 Fullerene is abbreviated as C60. Poly[[2,3-bis(3-octyloxyphenyl)-5,8-quinoxalinediyl]-2,5-thiophenediyl] is abbreviated as TQ1. Poly(3,4-ethylenedioxythiophene)-poly(styrenesulfonate) is abbreviated as PEDOT:PSS. Aluminium-doped zinc oxide is abbreviated as AZO.

The bismuth halide based compounds crystallize directly and rapidly into a textured polycrystalline microstructure from a precursor solution without evolving through intermediate crystalline solvated phases, as determined by multi-probes *in situ* characterization methods.[58] The maintenance of a continuous polycrystallinity within $MA_3Bi_2I_9$ films is crucial to the good performance of the resulting solar cells. Recently, some new methods have been applied for the preparation of $MA_3Bi_2I_9$ thin films. A highly compact, large grained $MA_3Bi_2I_9$ film can be prepared employing a two-steps approach based on the subsequent thermal evaporation of BiI_3 and MAI. By employing this method, an excellent PCE of 1.64% was achieved.[59] (Fig. 7a, b) The vapor assisted solution processing (VASP) method also allows the preparation of homogeneous $MA_3Bi_2I_9$ perovskite derivative films by exposing solution processed BiI_3 films to MAI vapors. Given the very good film quality obtained by applying this method, hysteresis-free *J-V* curves were recorded with an overall PCE of 3.17% on mesoporous TiO_2 ETLs, with excellent reproducibility (Fig. 7c, d).[60] This is one of the highest performances found among $MA_3Bi_2I_9$-based lead-free PvDSCs. The uniform and compact $MA_3Bi_2I_9$ thin film was prepared by a two-step (evaporation and spin-coating) and the inverted planar PvDSCs exhibited a PCE of 0.39%. More excitingly, the value of V_{oc} among the inverted $MA_3Bi_2I_9$ photovoltaic devices is up to 0.83 V.[61]

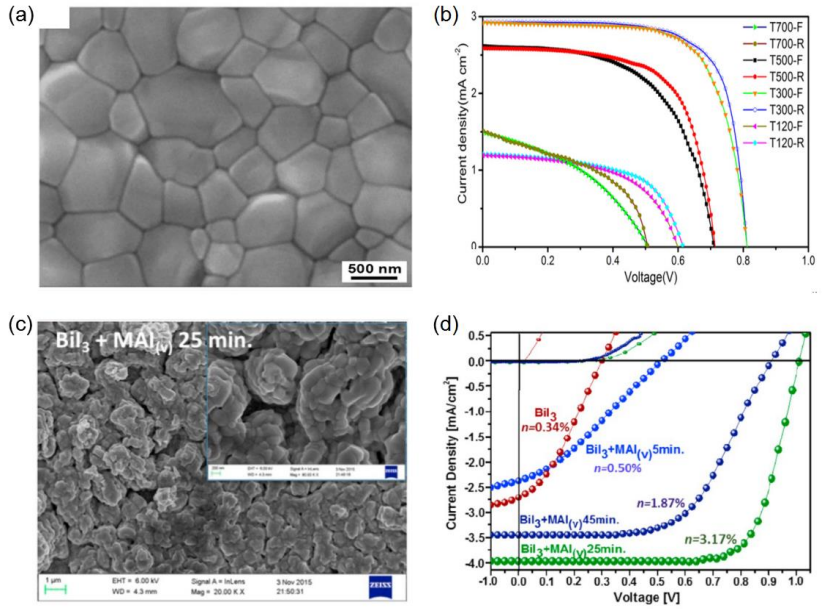

Fig. 7 (a) Top-view SEM image of a thermally evaporated $MA_3Bi_2I_9$ thin film. (b) *J-V* curves for the best PvDSC based on a $MA_3Bi_2I_9$ light absorber obtained employing different deposition conditions. Reproduced with permission.[59] Copyright 2017, American Chemical Society. (c) Top-view SEM image of VASP deposited $MA_3Bi_2I_9$ on mesoporous TiO_2. (d) *J-V* characteristics for BiI_3 and VASP-deposited $MA_3Bi_2I_9$. Reproduced with permission.[60] Copyright 2018, Elsevier.

In thin-film solar cells, the film morphology has a very important effect on the performance of device. Hence, a lot of work has been done to optimize the morphology of $MA_3Bi_2I_9$ perovskite derivative thin films. A homogeneous film of $MA_3Bi_2I_9$ was produced by adding 1-methyl-2-pyrrolidinone (NMP) to the $MA_3Bi_2I_9$-DMF precursor solution. By applying this modification to the processing, PCE of the resulting solar device reached 0.31% with high reproducibility. Devices also maintained stable figure of merits for up to 30 days in a relative humidity of 50-60%.[62] $MA_3Bi_2I_9$ perovskite derivative cuboids have been synthesized by an antisolvent assisted crystallization (ASAC) method. Fabricated mesoporous devices based on this species showed a 0.356% PCE and excellent stability to air for more than 60 days.[63]

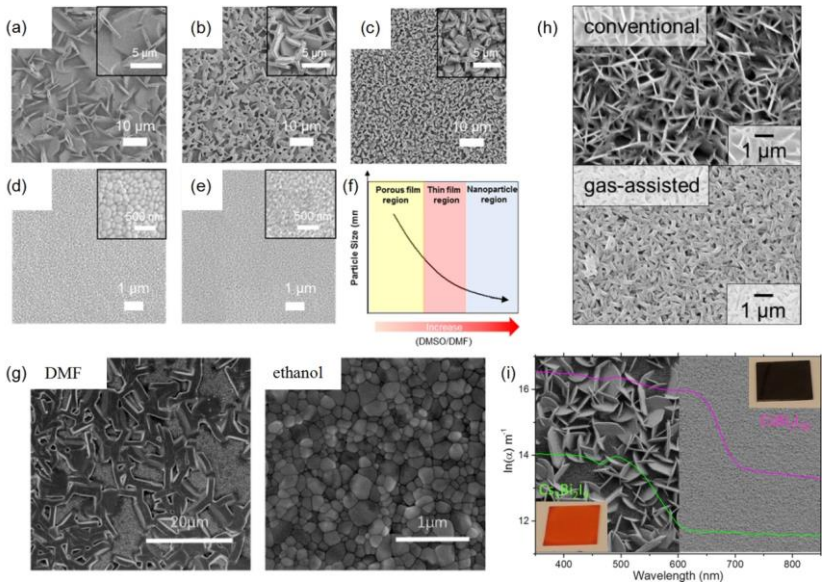

Fig. 8 Multiple top view SEM images of $MA_3Bi_2I_9$ films prepared through different methodologies. $MA_3Bi_2I_9$ film morphology depends on the amount of DMSO solvent added to DMF and on whether chlorobenzene (CB) is added. (a) DMF without CB, (b) DMF with CB, (c) DMSO:DMF = 0.05:0.95 (v:v) with CB, (d) DMSO:DMF = 0.2:0.8 (v:v) with CB, and (e) DMSO with CB. (f) $MA_3Bi_2I_9$ particles size and packing density curve with variation of the DMSO/DMF ratio. Reproduced with permission.[65] Copyright 2018, American Chemical Society. (g) $MA_3Bi_2I_9$ perovskite derivative films fabricated with DMF (left) and ethanol (right). Reproduced with permission.[66] Copyright 2017, Wiley VCH. (h) $MA_3Bi_2I_9$ films prepared via gas-assisted and conventional methods. Reproduced with permission.[67] Copyright 2017, Elsevier. (i) $Cs_3Bi_2I_9$ (right) and $CsBi_3I_{10}$ (left) film morphologies, color and absorption coefficients. Reproduced with permission.[74] Copyright 2016, American Chemical Society.

Shin et al. obtained compact thin films of $MA_3Bi_2I_9$, $Cs_3Bi_2I_9$, $FA_3Bi_2I_9$ by a solvent engineering method relying on different ratios for the DMSO/DMF solvent couple (Fig. 8a-e). Based on grain nucleation rates and growth rates, a mechanism for film formation has been proposed by the authors that considers the existence of three different regions for the final film morphology, namely a porous, a thin and a nanoparticle-like ones (Fig. 8f). PIF8-TAA, a co-polymer of triarylamine and benzo-fused difluorene units, was used to replace the classical spiro-OMeTAD,[64] allowing to reach a PCE of 0.71% in a $MA_3Bi_2I_9$ based PvDSC. More excitingly, the highest value for V_{oc} reported to date among the $MA_3Bi_2I_9$ photovoltaic devices was recorded, namely 0.85 V.[65] Dense and homogeneous $MA_3Bi_2I_9$ films can be obtained by employing ethanol as the solvent, differently from the porous and rough ones obtained with DMF (Fig. 8g). The PvDSC based on ethanol prepared $MA_3Bi_2I_9$ films showed a high V_{oc} of 0.84 V, a J_{sc} of 0.17 mA cm^{-2}, a FF of 0.35, and a PCE of 0.053%.[66] A dense and smooth $MA_3Bi_2I_9$ active layer was also prepared by a gas-assisted deposition method. Compared to the conventional one-step all solution-based method, a PCE improvement of 17% was obtained (Fig. 8h for a comparison of $MA_3Bi_2I_9$ film morphologies).[67] By further applying a fluorinated perylene diimide (FPDI) as ETL in a $MA_3Bi_2I_9$ PvDSCs, a limited PCE degradation (- 0.06%) was recorded when maintaining the devices in ambient atmosphere for 17 days.[68]

Lan et al. designed a $(BiI_3)_{1-x}(MA_3Bi_2I_9)_x$ mixed species with an optimized photovoltaic output. The $(BiI_3)_{0.8}(MA_3Bi_2I_9)_{0.2}$-based PvDSCs showed indeed an increase in V_{oc} from 0.44 to 0.57 V compared to the one based on pristine $MA_3Bi_2I_9$, with a PCE of 0.08%.[69] Song and coworkers compared the conventional one-

step solution processing for $MA_3Bi_2I_9$ with a two-step method based on the interdiffusion of solution-processed BiI_3 and CH_3NH_3I stacking layers, achieving a higher PCE with the latter approach in a mesoscopic PvDSC compared to the use of the former (0.29% *vs* 0.15%).[70] $MA_3Bi_2I_9$ PvDSCs have been also fabricated by Chen et al. employing a two-step solution process method on rutile TiO_2 nanorod array ETL. Although recorded PCE was still very low, devices didn't suffer any degradation of performance after 67 days of storage in ambient conditions.[71] A cation displacement approach was also employed to improve the morphology of $MA_3Bi_2I_9$ film. This consisted in first depositing from a solution of ethylammonium iodide and BiI_3 and then transforming the resulting hybrid material into $MA_3Bi_2I_9$ by keeping the film in a methylamine atmosphere. The $MA_3Bi_2I_9$ film has a smooth, uniform, and compact surface morphology. By employing it as light absorber in a mesoporous PvDSC architecture, a PCE of 0.33% was achieved, about two times higher than the value (0.15%) obtained with a one-step spin-coating method.[72]

High-quality ultrathin $Cs_3Bi_2I_9$ nanosheets have been developed by Zhang and coworkers employing a dissolution-recrystallization process and applied as light absorbers in PvDSC, obtaining an impressive PCE value of 3.20% when CuI was used as the HTL.[73] In order to optimize the photoelectric performance of $Cs_3Bi_2I_9$, Johansson et al. investigated a new type of cesium bismuth iodine compound of $CsBi_3I_{10}$. Compared to the band gap of 2.03 eV found for $Cs_3Bi_2I_9$, the $CsBi_3I_{10}$ film reached a value of 1.77 eV, with absorption maximum shifting from 610 nm to 700 nm (Fig. 8i). The absorption coefficients for $CsBi_3I_{10}$ increased as well by an order of magnitude compared to $Cs_3Bi_2I_9$. At last, the PCE of a PvDSC based on $CsBi_3I_{10}$ was 0.4% higher than that of the reference.[74] Subsequently, the group conducted further research on this material. By using dopant-free hole-conducting polymers, the energy mismatch between the $CsBi_3I_{10}$ film and the HTL materials was alleviated. Hence, a higher PCE was obtained for the modified device.[75] However, Khadka et al. fabricated solution processed $Cs_3Bi_2I_9$ and $CsBi_3I_{10}$ thin films via a solvent vapor annealing step. They found that the $Cs_3Bi_2I_9$ film has a wider bandgap (2.08 eV) than the $CsBi_3I_{10}$ one (1.8 eV), but it is more stable under annealing conditions. The $Cs_3Bi_2I_9$ film achieved a PCE as high as 1.26% for the resulting device. For comparison, the $CsBi_3I_{10}$ based PvDSC exhibits only poor efficiency.[76] Hence, we believe there are still many problems to be solved when $CsBi_3I_{10}$ is employed as light absorber in PvDSCs.

The layered polymorph of $Cs_3Bi_2Br_9$ was studied by Melot and coworkers experimentally and *via* DFT. The structure of this compound is a corrugated layer of corners sharing $BiBr_6^{3-}$ octahedra. An exciton binding energy of 940 meV is found, substantially higher than values found in other halide perovskite derivatives and closer to values seen in alkali halide crystals. This indicates a strongly localized exciton character and it is also the cause of a highly structured emission. Such a large exciton binding energy, coupled to a large band gap of 2.64 eV, is of course detrimental for a photovoltaic material and the compound requires further compositional engineering to be applied for this scope.[77] A single crystal of the $MA_3Bi_2Br_9$ perovskite derivative has been studied by Leng et al. and the compound resulted to display a trigonal symmetry (*P*3*m*1 space group), characterized by metal halide octahedral layers (Fig. 9a). The $MA_3Bi_2Br_9$ perovskite derivative has a direct bandgap of 2.5 eV and a photoluminescence quantum yield (PLQY) up to 12% when the material is in the form of quantum dots (λ_{em} max = 430 nm).[78] $FA_3Bi_2Br_9$ ~~perovskite derivative~~ quantum dots also exhibit a bright blue emission at 437 nm with a high PLQY of 52%.[79]

Four organic-inorganic bismuth halides (OIBHs) were also synthesized through a solvothermal method (Fig. 9b for details of the crystal structures). Halogens appear to change configurations in these bismuth halides. For example, $(TMP)[Bi_2I_5]$ (with TMP indicating the di-cationic molecule tetramethylpiperazine) with one single halide species shows a 1D chain structure, while $(TMP)_{1.5}[Bi_2I_7Cl_2]$, with mixed halogens (I and Cl) is a rare case of 2D structure. This compound is a potential light harvesting material because of the band gap of 2.10 eV, electrical conductivity of 2.37×10^{-6} S cm^{-1}, efficient photoconductivity and high stability under prolonged exposure to humid air or light.[80]

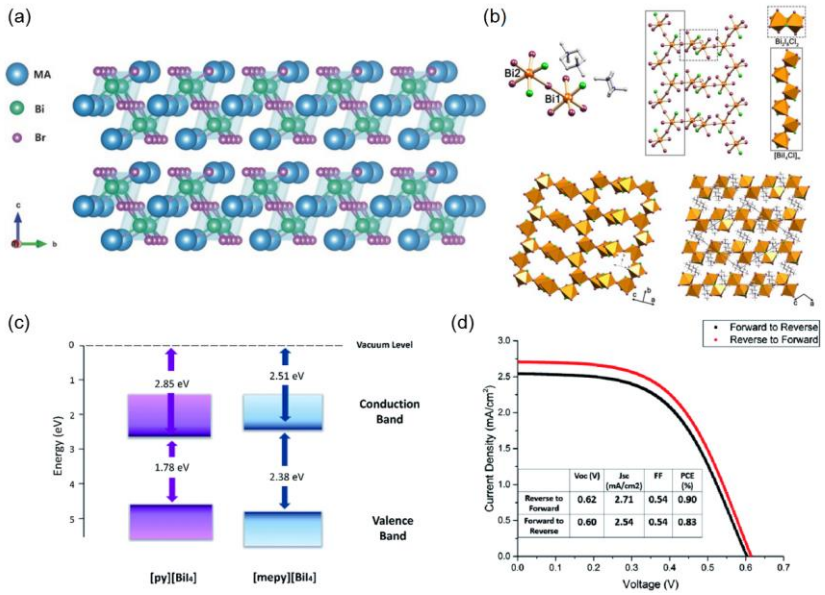

Fig. 9 (a) Crystal structure of single-crystalline $MA_3Bi_2Br_9$. Reproduced with permission.[78] Copyright 2016, Wiley VCH. (b) Four structures of $(TMP)_{1.5}[Bi_2I_7Cl_2]$. Reproduced with permission.[80] Copyright 2017, American Chemical Society. (c) Energy level diagram for [py][BiI_4] and [mepy][BiI_4]. (d) *J-V* curves of the [py][BiI_4]-based champion cell. Reproduced with permission.[23] Copyright 2017, the American Institute of Physics.

The properties of bismuth halides based perovskite derivatives can be partially regulated through halogen doping. $MA_3Bi_2I_9$ has been doped with Cl^- and a series of $MA_3Bi_2I_{9-x}Cl_x$ films were prepared. The mixed anion $MA_3BiI_{5.22}Cl_{3.78}$ employed as an absorption layer also provided a maximum PCE of 0.18%, with a high FF of almost 60% and an excellent long term stability of more than 700 days for devices stored under inert atmosphere.[81] In addition, the PCE of $MA_3Bi_2I_{9-x}Cl_x$ was found to raise with the increase of Cl^- doping content.[82] The low-pressure VASP method was applied to obtain a $MA_3Bi_2I_{9-2x}S_x$ perovskite derivative film. The sulfur incorporated in the perovskite derivative film leads to a reduced bandgap of 1.67 eV and a compact morphology. The optimal PCE for PvDSC based on this species reaches 0.152%.[83] We have also carried out some innovative works on the $Cs_3Bi_2I_9$ system.[84] $Cs_3Bi_2I_{9-x}Br_x$ perovskite derivative materials were prepared by $Cs_3Bi_2I_9$ doping with bromide. By systematically comparing the crystal structure, the band structure and absorbance of the $Cs_3Bi_2I_{9-x}Br_x$ materials (Fig. 10), we found that $Cs_3Bi_2I_6Br_3$ is the compound with the lowest bandgap (2.03 eV, with that of $Cs_3Bi_2I_9$ being 2.20 eV). More importantly, a phase transition from space group $P6_3/mmc$ to the $P\bar{3}m$ due to the presence of three bromide atoms was first identified in the system. At last, a champion device with a PCE of 1.15% was obtained based on a $Cs_3Bi_2I_6Br_3$ light absorbing layer.

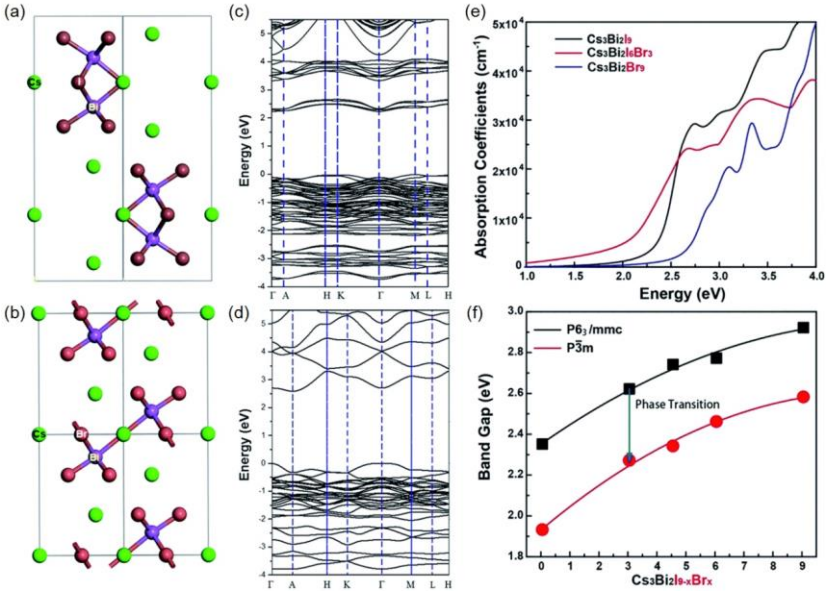

Fig. 10 The crystal structure of (a) $Cs_3Bi_2I_9$ and (b) $Cs_3Bi_2Br_9$, respectively. The calculated band structure of (c) $Cs_3Bi_2I_9$ and (d) $Cs_3Bi_2Br_9$, respectively. (e) The calculated absorbance of $Cs_3Bi_2I_9$, $Cs_3Bi_2I_6Br_3$ and $Cs_3Bi_2Br_9$ materials. (f) The variation of the band gaps in $Cs_3Bi_2I_{9-x}Br_x$ in the *P*6$_3$/*mmc* and the *P*$\bar{3}$*m* phases with the composition x. Reproduced with permission.[84] Copyright 2019, the Royal Society of Chemistry.

It is widely accepted that defect-sites in $A_3B_2X_9$-based PvDSC are responsible for the low PCE. In a relevant solid-state physics study, Pal and coworkers introduced the scanning tunneling spectroscopy (STS) method to understand the nature of defects in bismuth halides based ternary perovskite derivative systems. The band gap of $Cs_3Bi_2I_9$ prepared with BiI_3-rich precursor decreased from 2.01 eV employing the exact stoichiometric ratio to 1.81 eV, due to formation of mid-gap deep defects, as evidenced by such STS studies.[85] Hence, it is possible that the PCE of bismuth halides based PvDSC may be further improved by finding a method to passivate these defects.

Another 1D chain-like structure, $(H_3NC_6H_{12}NH_3)BiI_5$ (HDABiI$_5$), was synthesized from a non-toxic trivalent bismuth iodide and thermally stable 1,6-hexane diammonium groups. HDABiI$_5$ shows better thermal stability than lead-based perovskites (up to 200 ^oC), although still providing very low PCE in PvDSC, due to the relatively large band gap.[21]

Similar 1D chain-like organic-inorganic iodobismuthates, namely $C_5H_6NBiI_4$ ([py][BiI$_4$])(py: pyridinium) and $C_6H_8NBiI_4$ ([mepy][BiI$_4$]) (mepy: methylpyridinium), have been prepared by Sun et al. The organic moieties, constituted of protonated aromatic heterocycles, ensure the charge carriers transport in [py][BiI$_4$] and [mepy][BiI$_4$]. These compounds have band gaps of 1.78 eV and 2.38 eV, respectively. The efficiency of an HTL-free PvDSCs approached 0.9%, which is a good result for bismuth halides based hybrid perovskite derivative solar materials (Fig. 9c, d).[23] Additionally, a series of 1D chain-like Sb/Bi halides based organic-inorganic hybrid alloys of formula $[4ApyH]Sb_xBi_{1-x}IyBr_{4-y}$, where 4ApyH stands for the 4-aminopyridine cation, were synthesized. Among these systems, $[4ApyH]Sb_{0.8}Bi_{0.2}I_4$ and [4ApyH]SbI$_4$ provided detectable light to electricity conversion efficiencies of 0.29% and 0.30%, respectively.[86] Finally, a dense and pinhole-free $(C_6H_5NH_3)BiI_4$ film was fabricated using an eco-friendly gas pump treatment technique by Yang and

coworkers. The material can tolerate continuous moisture exposure for 334 days in ambient air, without significant degradation.[87]

4.1.2 Photovoltaics devices based on double perovskite structures

The $A_2B^IB^{III}X_6$ perovskites are characterized ~~by~~as a 3D structure ~~that encompasses~~with two kinds of B cations (B^I and B^{III}) ~~dominated perovskite cells, which are~~ adjacent to each other in the cubic phase. These $A_2B^IB^{III}X_6$ double perovskites usually show a high tolerance to defects, due to the strong ionic nature of the basic constituents. On the other hand, they unfortunately have large bandgaps compared to the lead-based reference, which limits the amount of light they can absorb from the solar spectra, coupled to high-exciton binding energies (intense excitonic peaks are often observed in absorption spectra of these compounds in thin films). The performances in bismuth halides based double PvSCs reported up to now are summarized in Table 2.

Table 2 Summary of performance for bismuth halides based double perovskite solar cells

Device structure	E_g (eV)	J_{sc} (mA/cm^2)	V_{oc} (V)	FF	PCE (%)	Ref.
FTO/SnO_2/$Cs_2AgBiBr_6$/P3HT/Au	2.05	1.78	1.04	0.78	1.44	[88]
FTO/TiO_2/meso-TiO_2/$Cs_2AgBiBr_6$/spiro-OMeTAD/Au	2.21	3.93	0.98	0.63	2.43	[89]
FTO/TiO_2/$Cs_2AgBiBr_6$/Spiro-MeOTAD/Au	1.95	1.55	1.06	0.74	1.22	[90]
FTO/TiO_2/meso-TiO_2/$Cs_2AgBiBr_6$/PTAA/Au	2.10	1.84	1.02	0.67	1.26	[91]
FTO/TiO_2/$Cs_2AgBiBr_6$/P3HT/Au	2.05	1.79	1.12	0.68	1.37	[92]
FTO/Cu-NiO_2/$Cs_2AgBiBr_6$r/C60/BCP/Ag	2.05	3.19	1.01	0.69	2.23	[93]
FTO/TiO_2/meso-TiO_2/$Cs_2AgBiBr_6$/N719/spiro-OMeTAD/Au	2.02	5.13	1.06	0.52	2.84	[94]
FTO/TiO_2/meso-TiO_2/Cs_2NaBiI_6/spiro-OMeTAD/Au	1.66	1.99	0.47	0.44	0.42	[95]

Note: (di-tetrabutylammonium *cis*-bis(isothiocyanato) bis(2,2′-bipyridyl-4,4′ dicarboxylato) ruthenium (II)) is abbreviated as N719.

Thus far, reports on fabrication of solar cells based on these halide double perovskites are rather limited, but their promising optoelectronic properties make us optimistic on their future and fruitful implementation in photovoltaics. Reports disclosing the optoelectronic properties of halide double perovskites of formula $A_2B^IB^{III}X_6$ demonstrate the excellent features of these materials, similar to those of their 3D $APbX_3$ counterparts. Bi^{3+} is the most commonly used trivalent cation in double perovskites, because it has the same isoelectronic configuration as Pb^{2+} ($6s^26p^0$) as mentioned above, and its toxicity is significantly reduced. For the B site, Ag^+, K^+, Na^+ or Tl^+ are the main monovalent cations that have been used so far, making them suitable for octahedral coordination.

The main breakthroughs obtained with double perovskite absorbers in PvSCs are summarized in the following lines. A low-pressure assisted solution method was used to prepare high-quality $Cs_2AgBiBr_6$ double perovskite for the first time. Excitingly, a device based on such a lead-free absorber showed excellent thermal and ambient stability without the need for encapsulation. Annealing temperatures of 250 ºC are required to obtain a full conversion from the precursors to $Cs_2AgBiBr_6$. The corresponding planar heterojunction device based on $Cs_2AgBiBr_6$ reached a best PCE value of 1.44%.[88] Another reported photovoltaic device exhibited a PCE close to 2.5%, with J_{sc} of 3.93 mA cm^{-2}, V_{oc} of 0.98 V, and FF of 0.63 (Fig. 11a, b). Furthermore, compared to $MAPbI_3$, a test under constant illumination showed that the resistance to degradation is very high when the cells are maintained in environmental conditions, and no PCE degradation was found to occur after 25 days.[89] A uniform $Cs_2AgBiBr_6$ thin solid film was fabricated by a simple one-step spin coating method. This high-quality double perovskite film enabled the fabrication of planar PvSCs featuring long electron-hole diffusion lengths (more than 100 nm). An average PCE over 1% was achieved by employing a planar TiO_2 ETL.[90] Pantaler et al.

reported also hysteresis-free mesoporous double PvSCs base on the $Cs_2AgBiBr_6$ absorber. A maximal PCE of 1.26% was recorded using PTAA as the HTL.[91]

New ideas have been developed to improve the performance of double perovskites-based devices. $Cs_2AgBiBr_6$ thin films were prepared through a sequential vapor deposition procedure (Fig. 11c). The obtained films exhibited large grain sizes and uniform, smooth surface properties. The solar cells with planar structure showed a PCE of 1.37% and an excellent stability to standard environmental conditions (Fig. 11d).[92] A high quality $Cs_2AgBiBr_6$ film was further realized via an anti-solvent dropping technology, followed by an annealing step. An inverted planar heterojunction PvSC based on this film exhibits a PCE of 2.23%.[93] Recently, a multifunctional N719 dye interlayer was introduced in $Cs_2AgBiBr_6$ PvSCs for improving the PCEs and stability.[94] The device showed a PCE of 2.84%, which was the top PCE for a double PvSCs reported so far.

Moreover, a new lead-free double perovskite material of formula Cs_2NaBiI_6 was synthesized and applied in PvSC. A narrow band gap of 1.66 eV and the excellent stability have been found in such a shuttle-like 3D Cs_2NaBiI_6 material. Experimental tests have been carried out for Cs_2NaBiI_6 based PvSCs, obtaining a best PCE of 0.42%, a value comparable to those of other bismuth halides based double PvSCs.[95]

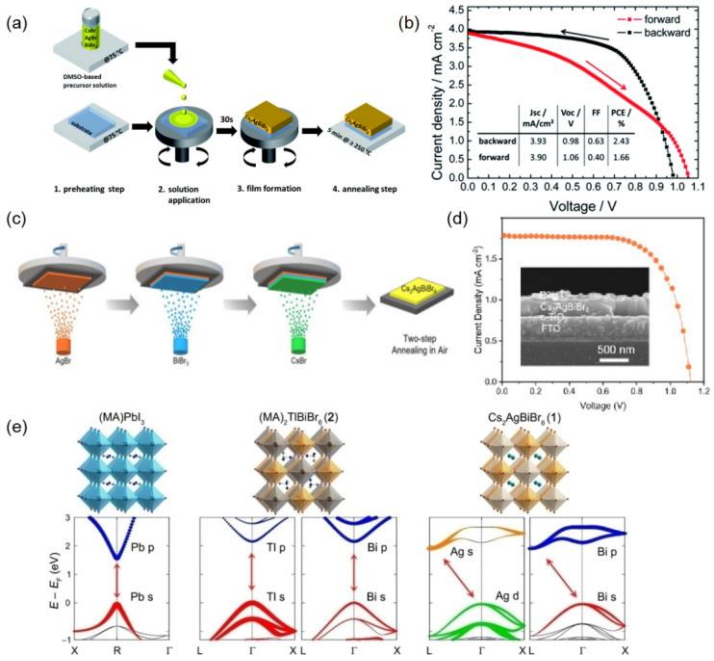

Fig. 11 (a) Scheme depicting a tested preparation route for $Cs_2AgBiBr_6$ thin films. (b) *J-V* curve of the best performing device prepared as in (a). Reproduced with permission.[89] Copyright 2017, the Royal Society of Chemistry. (c) Scheme for the sequential vapor deposition processing of $Cs_2AgBiBr_6$ thin films. (d) *J-V* curve of the optimized solar cell prepared as in (c). Inset: cross-sectional SEM image of the resulting device. Reproduced with permission.[92] Copyright 2018, Wiley VCH. (e) Crystal structures and band structures of $MAPbI_3$, $(MA)_2TlBiBr_6$, and $Cs_2AgBiBr_6$. Arrows showing the direct (left and center) and indirect (right) bandgap transitions. Reproduced with permission.[96] Copyright 2017, American Chemical Society.

Compositional tuning efforts have also been made to decrease the band gap of double perovskite materials. Recently, Tl was added to $Cs_2AgBiBr_6$ as an impurity to form opaque black crystals with structure $Cs_2(Ag_{1-a}Bi_{1-b})Tl_xBr_6$. The content of Tl was varied from 0.03% to 0.75%. Tl cations can replace both Ag^+ (as Tl^+) and Bi^{3+} (as Tl^{3+}) sites, as demonstrated by theoretical and experimental studies. At higher concentrations of Tl, the replacement of Ag^+ is preferable. The reflectivity measurements clearly show that the experimental bandgap decreases with an increase in Tl content, with a minimum value of 1.57 eV at x = 0.075. When Tl^{3+} replaces Bi^{3+}, a new lower energy conduction band with Tl 6s and Ag 4d character is formed, which reduces the band gap energy and leads to an indirect transition, as predicted by DFT. When Tl^+ substitutes Ag^+, the Tl 6p states together with Br 4p and Bi 6p states form a new conduction band with lower energy that generates a direct transition, as shown in Fig. 11e.[96] A similar bandgap engineering of $Cs_2AgBiBr_6$ was also carried out by introducing Sb^{3+} via a versatile solution-based method. The Sb-substitution enables an obvious reduction of the bandgap of 0.25 eV.[97] In addition, two other hybrid double perovskites, $(MA)_2TlBiBr_6$ and $(MA)_2AgBiBr_6$ have been synthesized, with interesting optoelectronic properties. Both double perovskites were prepared through the hydrothermal method and crystallized in the same cubic space group *Fm*3*m*. In agreement with what prospected by DFT, the direct band gap of $(MA)_2TlBiBr_6$ was experimentally found to be 2.16 eV.[98] Tl does not change the crystal momentum of the valence and conduction bands, hence maintaining the same strong absorption ability of $APbX_3$ materials. However, $(MA)_2TlBiBr_6$ contains Tl, a highly toxic element that may limit its use as a substitute for photovoltaics materials. On the other hand, similar to $Cs_2AgBiBr_6$, $(MA)_2AgBiBr_6$ has an indirect band gap of 2.02 eV.[99]

The indirect character of the electronic transitions of the double perovskites leads to the initially discussed significant drawbacks of these materials, namely the low absorption coefficient and high exciton binding energy. The orbital interaction between monovalent B^I and trivalent B^{III} species in the marginal zone generally involves the movement of the conduction band minimum (CBM) and valence band maximum (VBM), leading to an indirect gap. By band gap engineering, indirect semiconductors can be converted into direct semiconductors by adjusting the relative proportions of the trivalent B^{III} cations.[100]

Other main disadvantages of the double perovskites seem to be related to the difficulties in employing solution-processing to fabricate highly crystalline films. More systematic studies are required to fabricate dense films. It is well-known that thermal evaporation under vacuum conditions is a good method compared to spin coating. Powder or single crystal of the double perovskite compound synthesized by hydrothermal method can be used as the starting material.

Recently, our group made use of the capillary-assisted dip-coating method to produce large-area, single-crystalline $Cs_2AgBiBr_6$ films.[101] The fabrication process of highly oriented $Cs_2AgBiBr_6$ films is shown in Fig. 12a, and this method can be applied to various substrates. The obtained optimized films are single crystalline, as verified by φ-scan XRD (Fig. 12c, d). The substrate lift speed is responsible for the final crystal habit of the films (Fig. 12e-g). By changing the substrate growth temperature, the bandgaps of the thin films can be tuned from 2.65 to 2.25 eV. By DFT calculations, it was further possible to highlight that the band structure of these films displayed a typical n-type characteristic. Our results show that the deep defects around the Fermi level are Cs interstitials and Br vacancies. This method offers new directions for the preparation of double perovskite thin films, which might bring a step-change in overall device performances.

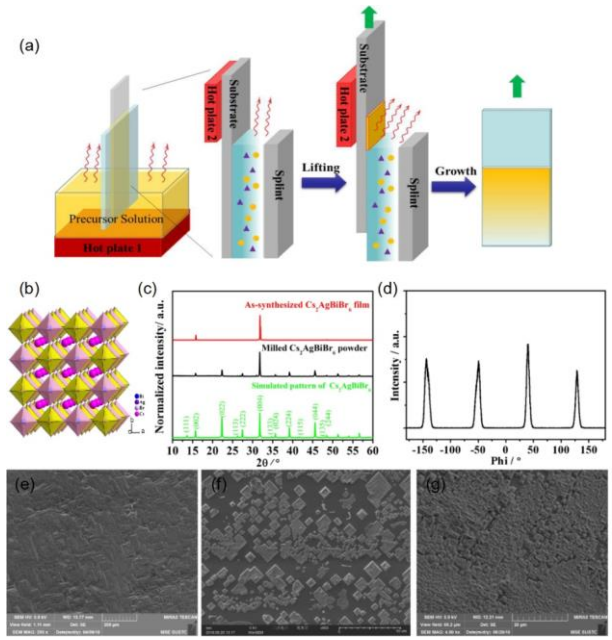

Fig. 12 (a) Schematic illustration of the Capillary-assisted Dip Coating process used for the production of $Cs_2AgBiBr_6$ films. (b) Schematic structure of the cubic double perovskite $Cs_2AgBiBr_6$. (c) XRD patterns of an as synthesized $Cs_2AgBiBr_6$ film and powder. (d) ϕ-scan XRD pattern of the as synthesized $Cs_2AgBiBr_6$ film. Top-view SEM images of $Cs_2AgBiBr_6$ films prepared by applying a lifting speed of 10 µm/s (e), 50 µm/s (f) and 25 µm/s (g). Reproduced with permission.[101] Copyright 2019, Elsevier.

4.2 Antimony based halide perovskite and their derivatives solar cells

Similar to Bi, Sb can also form different combinations with organic/inorganic cations and halides, as discussed in Section 2.2.[102] Among them, the $Cs_3Sb_2I_9$ and $MA_3Sb_2I_9$ compounds are the mostly investigated in the context of photovoltaics research. Table 3 summarizes the photovoltaic performance of solar energy conversion devices based on antimony based halide perovskite derivative materials.

According to the synthetic conditions, $Cs_3Sb_2I_9$ can form different solid-state structures. When prepared from solution, $Cs_3Sb_2I_9$ prefers to form a 0D structure with isolated dimers of face sharing octahedra ($P6_3/mmc$). The formation of 2D layered structures takes place during solid or gas reactions (space group $P\bar{3}m1$). $Cs_3Sb_2I_9$ thin films preparation and characterization was reported in 2015, together with the first solar cell employing this compound as the light absorber. $Cs_3Sb_2I_9$ thin film prepared via a two-steps deposition method have a red color layered structure, differently from the orange color of 0D $Cs_3Sb_2I_9$. The band gap of the 2D $Cs_3Sb_2I_9$ thin film results to be 2.05 eV, with an absorption coefficient of 10^5 cm^{-1} and a ionization energy of 5.6 eV, as reported by Saparov et al.[10] The stability of the thin films in ambient air is better than that of $MAPbI_3$ films. Due to nonradiative recombination caused by the presence of deep defects, the performance of $Cs_3Sb_2I_9$-based PvDSCs is very low (below 1%) and the V_{oc} is between 0.25 and 0.3 V. The 0 D $Cs_3Sb_2I_9$ structure with a band gap of 2.0 eV was also applied in planar PvDSCs. When HI was employed as additive, the devices showed a champion PCE of 0.84%, with a V_{oc} of 0.60 V.[103] Correa-Baena et al. reported that the 0 D $Cs_3Sb_2I_9$ is an indirect bandgap semiconductor with a large exciton binding energy, which explained the low photocurrent and PCE.[29] A

layered polymorph and a dimeric form of $Cs_3Sb_2I_9$ were prepared *via* vapor-assisted solution processing. The measured exciton lifetime and binding energy for the layered $Cs_3Sb_2I_9$ resulted to be 6 ns and 100 meV, respectively. The layered and the dimeric $Cs_3Sb_2I_9$ forms used in PvDSC provided PCE of 1.5 and 0.89%, respectively.[104] Meanwhile, Zhou et al. also prepared high-quality ~~perovskite derivative~~ films composed of the perovskite derivative layered phase $MA_3Sb_2Cl_xI_{9-x}$ by adding methylammonium chloride into the precursor solutions.[105]

As mentioned above, $Cs_3Sb_2I_9$ films prepared through solution processing are more inclined to organize in the dimeric form. To solve this problem, we have also carried out pioneering investigations in the area.[106] Hydrochloric acid (HCl) as an additive was introduced into the precursor solution. In this way, chloride acted as in inhibitor in the reaction, slowing down the formation of Sb-I-Sb bond. Hence, a layered $Cs_3Sb_2I_9$ film was developed from an intermediate coordinated phase using this HCl-assisted strategy (Fig. 13a). From a series of characterizations, the bandgap of the layered compound results to be 2.05 eV, thus smaller than that of the dimeric one, ~ 2.47 eV (Fig. 13b). The all inorganic layered $Cs_3Sb_2I_9$ device showed a top PCE value of 1.21%, while the dimer-based device only acquired a PCE of 0.43% (Fig. 13c). The PCE improvement in the layered $Cs_3Sb_2I_9$ thin films is due to lower trap density, doubled carrier mobility and improved junction quality, as determined by space-charge-limited-current measurement (Fig. 13d, e). Through the addition of HCl, the problem that with solution method is easier to form the dimeric form can be effectively solved. We believe that this novel method will greatly promote the fast progress of $Cs_3Sb_2I_9$-based lead-free PvDSCs.

Formattato: Evidenziato

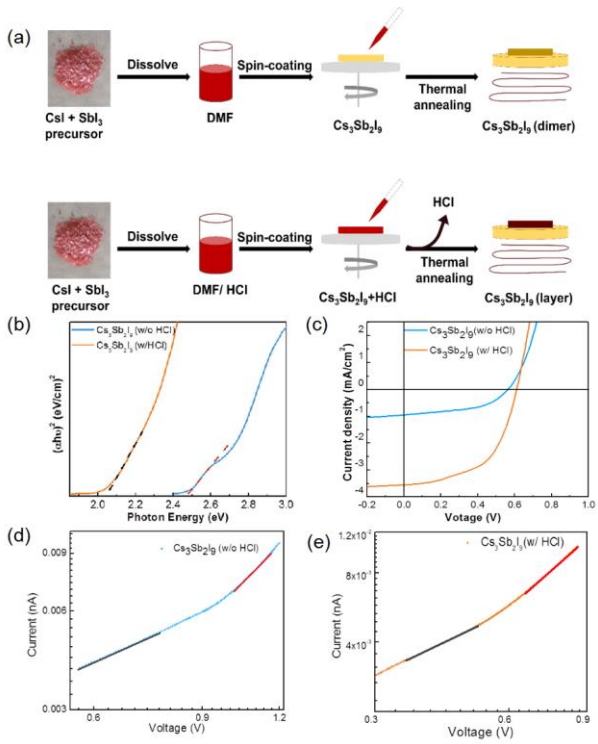

Fig. 13 (a) Schematic representation of the anti-solvent solution method used by us for the preparation of layered and dimeric $Cs_3Sb_2I_9$ thin films. (b) Calculated bandgaps from Tauc Plot of dimeric and layered phases. (c) *J-V* curves of PvDSC containing the two forms of the $Cs_3Sb_2I_9$ absorber. *J-V* scans of dimeric $Cs_3Sb_2I_9$ thin films (d) and of layered one (e). Reproduced with permission.[106] Copyright 2019, Wiley VCH.

In addition to our HCl-assisted method, the introduction of alkalis can also regulate the electronic structure of $Cs_3Sb_2I_9$ film. A lot of work in this respect has been done. Harikesh et al. found that this compound can easily form layered structures *via* solution methods when Cs is replaced by Rb (Fig. 14a). With the help of DFT, they compared the formation energies of the dimeric and layered forms of $A_3Sb_2I_9$ with A = Cs and Rb. Compared to the ionic radius of Cs (1.88 Å), that of Rb (1.72 Å) is smaller and therefore $Rb_3Sb_2I_9$ is more prone to feature the layered phase. In addition, $Rb_3Sb_2I_9$ has better heat resistance compared to the analogous Cs compound, a favorable property for an efficient solar cell operation. Unfortunately, the $Rb_3Sb_2I_9$ semiconductor has an indirect bandgap of 2.1 eV, and PvDSCs based on it employing poly-TPD as the HTL were found to provide poor figure of merit, namely, a J_{sc} of 2.11 mA cm^{-2}, a V_{oc} of 0.55 V and PCE of only 0.66 %.[107] $A_3Sb_2I_9$ thin film in which the A site cation was Cs, Rb, and K were prepared by solution-processing to be used for photovoltaics. The A-site cation has an important effect on the structural and optoelectronic properties of these thin films. The large exciton binding and carrier effective masses of $A_3Sb_2I_9$ give rise to low photocurrents. A maximum PCE of 0.76% was recorded when $Rb_3Sb_2I_9$ was employed as the absorber.[29] Weber et al. found that the crystalline lattice does not change when the smaller bromide is used to substitute iodide. On the other hand, the absorption onset appears blue shifted, with a band gap rising from 2.02 to 2.46 eV. In this work, solar cells based on the $Rb_3Sb_2I_9$ absorber displayed a PCE of 1.37%, the top efficiency recorded of a $Rb_3Sb_2I_9$ based PvDSC.[108]

Unlike the inorganic $A_3Sb_2I_9$, that often forms two different structures (the layered and dimeric ones), when using an organic cation such as MA^+, the antimony halides based perovskite derivatives of formula $MA_3Sb_2I_9$ only forms a 0D dimeric structure, with MA^+ cations surrounded by octahedric anionic metal halide units $(Sb_2I_9)^{3-}$. Hebig et al. first reported $MA_3Sb_2I_9$ as an absorber material in PvDSC. $MA_3Sb_2I_9$ have an optical band gap of 2.14 eV and an absorption coefficient $\alpha \approx 10^5$ cm^{-1}. Experiments indicate the presence of a large energetic disorder in $MA_3Sb_2I_9$ film. Furthermore, due to the low photocurrent, the device achieved a PCE of only 0.5%.[32] The single step method was used to prepare $MA_3Sb_2I_9$ films through solution processing. It is worth noting that HI as an additive may improve the quality of antimony halides based perovskite derivative film. The molar ratios of precursors and the concentration of HI were optimized, to reach a PCE of 2.04% on a planar architecture device.[103] The fabricated $MA_3Sb_2I_9$ PvDSC prepared with two-step procedure also shows good performance with a remarkable V_{oc} of 740 mV.[109] $MA_3Sb_2I_9$ surface morphology significantly influences the recorded PCE. Recently, large grain $MA_3Sb_2I_9$ crystals were prepared by inserting a hydrophobic scaffold, such as perylene and pyrene, into the precursor solution (Fig. 14b). Films with improved quality and decreased number of voids were obtained. Using these films as absorbers, a record efficiencies of 2.77% was obtained (Fig. 14c).[110] Dai et al. produced high-quality two-dimensional $MA_3Sb_2I_{9-x}Cl_x$ film by introducing bis(trifluoromethane)sulfonamide lithium (LiTFSI) to control the dimensional transformation. By this method, antimony halides based PvDSCs further achieved a PCE of 3.34%, which is the highest recorded PCE for pure antimony halides based PvDSCs.[111]

Table 3 Summary of the photovoltaic performance of solar cells based on antimony halides perovskite derivative light absorbers

Device structure	E_g (eV)	J_{sc} (mA/cm^2)	V_{oc} (V)	FF	PCE(%)	Ref.

FTO/TiO_2/meso-TiO_2/$Cs_3Sb_2I_9$/spiro-OMeTAD/Au	2.43	0.13	0.40	0.58	0.03	[29]
ITO/PEDOT:PSS/$Cs_3Sb_2I_9$/PCBM/C60/BCP/Al	2.00	2.91	0.60	0.48	0.84	[103]
ITO/PEDOT:PSS/$Cs_3Sb_2I_9$/PCBM/Al	2.05	2.82	0.77	0.41	0.89	[104]
ITO/PEDOT:PSS/$Cs_3Sb_2I_9$/PCBM/Al	2.05	5.31	0.72	0.39	1.50	[104]
FTO/TiO_2/$Cs_3Sb_2I_9$/Au	2.05	3.55	0.61	0.56	1.21	[106]
FTO/TiO_2/meso-TiO_2/$K_3Sb_2I_9$/spiro-OMeTAD/Au	2.02	0.41	0.34	0.50	0.07	[29]
FTO/TiO_2/meso-TiO_2/$Rb_3Sb_2I_9$/spiro-OMeTAD/Au	2.03	1.84	0.66	0.63	0.76	[29]
FTO/TiO_2/meso-TiO_2/$Rb_3Sb_2I_9$/spiro-OMeTAD/Au	2.24	2.11	0.55	0.57	0.66	[107]
FTO/TiO_2/meso-TiO_2/$Rb_3Sb_2I_9$/spiro-OMeTAD/Au	2.02	4.25	0.55	0.60	1.37	[108]
ITO/PEDOT:PSS/$MA_3Sb_2I_9$/PCBM/C60/BCP/Al	1.95	5.41	0.62	0.61	2.04	[103]
FTO/PEDOT:PSS/Pyrene/$MA_3Sb_2I_9$/PCBM/C60/Al	1.90	6.64	0.7	0.60	2.77	[110]
FTO/TiO_2/m-TiO_2/$MA_3Sb_2I_{9-x}Cl_x$/Spiro-OMeTAD/Au	2.17	5.04	0.69	0.63	2.19	[105]
FTO/TiO_2/$MA_3Sb_2I_{9-x}Cl_x$ /Spiro-OMeTAD/ Au	1.89	7.38	0.70	0.65	3.34	[111]
ITO/Cu:NiO/ $MA_3(Sb_{1-x}Sn_x)_2I_9$/ZnO /Al	1.55	8.32	0.56	0.58	2.70	[112]
FTO/TiO_2/meso-TiO_2/$MASbSI_2$/PEPDTBT/Au	2.01	8.12	0.65	0.59	3.08	[114]
ITO/PEDOT:PSS/$(NH_4)_3Sb_2I_xBr_{9-x}$ /PCBM/Al	2.27	1.15	1.03	0.42	0.51	[115]
FTO/TiO_2/ $FA_4GeSbCl_{12}$/spiro-OMeTAD/Au	1.30	23.1	0.65	0.31	4.70	[117]

Note:(poly(2,6-(4,4-bis-(2-ethylhexyl)-4H-cyclopenta[2,1-b;3,4-b']dithiophene)-alt-4,7(2,1,3-benzothiadiazole)) is abbreviated as PEPDTBT.

Currently, some works have been carried out to reduce the band gap of $MA_3Sb_2I_9$ through element doping or replacing cation or anion. Pal et al. reported the lowered optical bandgap of $MA_3Sb_2I_9$ from 2 eV to 1.55 eV by introducing Sn^{4+} in the $MA_3Sb_2I_9$ structure. In addition, the conduction band edge of the perovskite derivatives gradually shifts towards a n-type Fermi level, due to the heterovalent substitution in $MA_3Sb_2I_9$. With an increase in the tin content, STS and density of state spectra indicate that the type of electronic conductivity should be tuned from p-type to n-type. However, the decrease of bandgap is at the expenses of an increased surface roughness for the films. The tin content was optimized to find a trade-off between a low band gap and a small surface roughness of the thin films. In this way, a planar heterojunction PvDSC was able to provide an excellent J_{sc} of 8.32 mA cm^{-2} and a PCE of 2.69%.[112] Methylammonium antimony sulfur diiodide ($MASbSI_2$) was fabricated for the first time as light harvester for photovoltaic application.[113] The $MASbSI_2$ compound was prepared by a sequential reaction, which was based on first processing Sb_2S_3 by chemical bath deposition and then SbI_3 and MAI through multiple cycles of spin coating and thermal annealing in argon (Fig. 14d). The solar cell based on $MASbSI_2$ showed an excellent PCE of 3.08% (Fig. 14e).[114] New perovskite derivative materials of formula $(NH_4)_3Sb_2I_xBr_{9-x}$ (0< x <9) were also developed. The light absorption maximum of these materials can be tuned from 558 to 453 nm. Single crystals of $(NH_4)_3Sb_2I_xBr_{9-x}$ show a hole mobility of 4.8 $cm^2V^{-1}s^{-1}$ and an electron mobility of 12.3 $cm^2V^{-1}s^{-1}$. A high V_{oc} of 1.03 V and a PCE of 0.51 % were acquired in $(NH_4)_3Sb_2I_xBr_{9-x}$ PvDSC.[115]

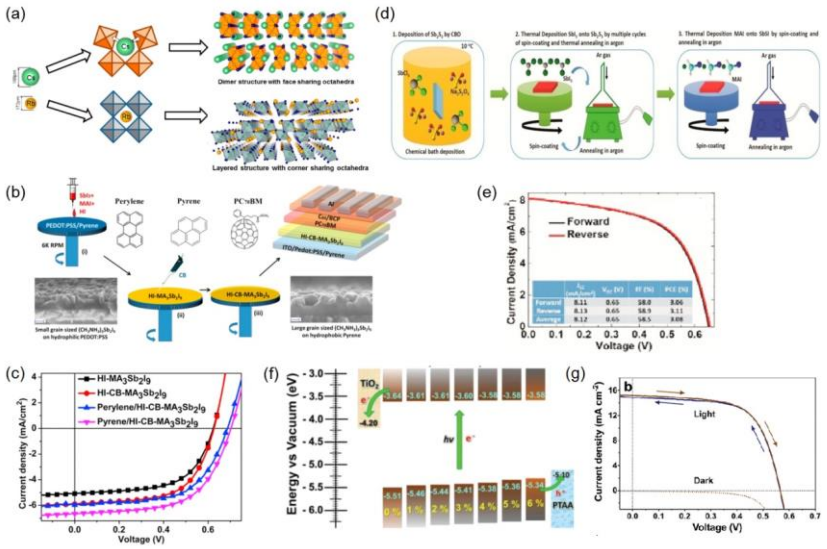

Fig. 14 (a) Schematic representation showing the influence of the A cation size on the structure of $A_3Sb_2I_9$. Reproduced with permission.[107] Copyright 2016, American Chemical Society. (b) Schematics of the deposition of HI-$MA_3Sb_2I_9$ thin films with hydrophobic organic additives, and cross-sectional SEM image of devices containing them. (c) *J-V* curve of Sb-based PvDSCs prepared as depicted in (b). Reproduced with permission.[110] Copyright 2018, Elsevier. (d) Process for preparing the $MASbSI_2$ ~~perovskite derivative~~ layer. (e) *J-V* curves in forward and reverse scan mode of the best performing $MASbSI_2$ PvDSC. Reproduced with permission.[114] Copyright 2018, American Chemical Society. (f) Diagram showing the electronic structure at different x of $Ag_3BiI_{6-2x}S_x$. (g) *J-V* curve of $Ag_3BiI_{6-2x}S_x$ -based PvDSCs with almost no hysteresis. Reproduced with permission.[121] Copyright 2019, Wiley VCH.

Antimony halides based double perovskite materials are a viable platform for the development of lead-free PvSCs and for this reason have attracted a significant attention in the last 5 years. Sb partial substitution has also been explored, as in the case of a layered perovskite of formula $Cs_4CuSb_2Cl_{12}$, where one Sb^{3+} ion was substituted with Cu^{2+}. The material has a direct bandgap of 1.0 eV and a high photo- and thermal stability.[116] Karmakar et al. also reported Cu^{2+} doped $Cs_2SbAgCl_6$, showing a decreased optical indirect bandgap from 2.6 eV to 1.0 eV. The Cu-doped material exhibited long term structural and photophysical stability up to 1 year, when it was maintained in thermal and moisture stress conditions.[33] Based on the principles of increased electronic dimensionality, by inserting $[M^{II}X_6]$ octahedra layers into $Cs_3Sb_2X_9$, a layered double perovskite family of $Cs_{3+n}M(II)_nSb_2X_{9+3n}$ (M = Sn, Ge) can be designed. Compared to $Cs_3Sb_2X_9$, the double perovskites have smaller bandgaps and smaller carrier effective masses. These parameters can be tuned by inserting different thickness of octahedral layers.[34] Recently, the $FA_4GeSbCl_{12}$ double perovskite has also been demonstrated to be a stable and efficient semiconductor with a direct bandgap of 1.3 eV. $FA_4GeSbCl_{12}$ based PvSCs were prepared to achieve the PCE up to 4.7%, without the use of any additive.[117]

4.3 Photovoltaic devices based on Rudorffite structures

3D materials are more favorable for photovoltaic applications than 2D species, in view of the lower bandgaps, smaller exciton binding energies and longer exciton diffusion lengths. Silver iodobismuthate compounds have been investigated as lead-free semiconductors in PvDSCs in recent years.[118] Sargent and coworkers reported a new solution-processed material of formula $AgBi_2I_7$. $AgBi_2I_7$ has a cubic

structure, which introduces monovalent silver cations into an iodobismuthate structure. The thin films have a dense and pinhole-free surface morphology and a bandgap of 1.87 eV. In PvDSC, this material allows to reach a PCE of 1.22% and an excellent environmental stability.[119] Ag-Bi-I Rudorffites are indeed potential non-toxic photovoltaic materials and for this reason have been investigated.[120] When Ag_3BiI_6 was used as the light absorber, the resulting solar cell provided a PCE of 4.3%.[28] The optoelectronic properties of $Ag_aBi_bI_{a+3b}$ have been further tuned by partial substitution with disulfide anions. $Ag_aBi_bI_{a+3b}$ was modified with sulfur, reducing the bandgap by 0.1 eV and upshifting the valence band edge by 0.1 - 0.3 eV (Fig. 14f). The resulting solar cells exhibited a PCE of 5.51% and good stability under ambient conditions for over 1 month (Fig. 14g).[121] Ag_2BiI_5 PvDSCs with PCE above 2.5% were also fabricated in air by a dynamic hot casting technique.[122]

A copper bismuth iodide ($CuBiI_4$) was prepared *via* a solution method. The material has a wide bandgap of 2.67 eV and its PvDSC provides a low PCE of 0.82%, but shows excellent long-term stability when maintained for over 40 days in ambient conditions.[123] Zhang reported a highly facile route for the *in-situ* production of $CuBiI_4$ with a favorable band gap of 1.81 eV. PvDSC displayed good photovoltaic performance with a PCE of 1.119%.[124] Device performance parameters for the light absorbers discussed in this paragraph are summarized in Table 4.

Table 4 Summary of performance for Rudorffite structure based PvDSCs

Device structure	E_g (eV)	J_{sc} (mA/cm^2)	V_{oc} (V)	FF	PCE (%)	Ref.
FTO/TiO_2/meso-TiO_2/ $Ag_3Bi_2I_6$/P3HT/Au	1.83	10.70	0.63	0.64	4.30	[28]
FTO/TiO_2/meso-TiO_2/$AgBi_2I_7$/P3HT/Au	1.87	3.30	0.56	0.67	1.22	[119]
FTO/TiO_2/meso-TiO_2/Ag_2BiI_5/P3HT/Au	1.85	6.80	0.49	0.63	2.10	[120]
FTO/TiO_2/meso-TiO_2/$Ag_3BiI_{6-2x}S_x$ /PTAA/Au	1.80	14.70	0.57	0.66	5.51	[121]
FTO/TiO_2/meso-TiO_2/Ag_2BiI_5/P3HT/Au	1.80	6.04	0.69	0.62	2.60	[122]
FTO/TiO_2/$CuBiI_4$/Spiro-OMeTAD/Au	2.67	2.19	0.63	0.57	0.82	[123]
ITO/$CuBiI_4$/Spiro-OMeTAD/Au	1.81	7.18	0.38	0.29	1.12	[124]

5. Conclusions and Outlook

In this review, we have summarized the structure, theoretical prediction, preparation methods and photovoltaic performances of several lead-free group VA Bi and Sb based halide species. The recent progress on $A_3B_2X_9$ or Rudorffite perovskite derivatives structures and double perovskite structures were in particular collected and discussed.

As for $A_3B_2X_9$ halides, it is worthy to remind here that the photovoltaic performance is closely related to the chameleonic structural and electronic dimensions. 0-D dimeric species or vacancy-ordered perovskite derivatives (2D) are generally unfavorable for optoelectronic applications. Their exciton binding energies are indeed relatively large and exciton diffusion lengths are short. Some new materials may hold great potential to solve these problems. For example, compounds like 2D $Rb_3Sb_2I_9$ or $Cs_3BiI_6Br_3$, can undergo an increase in lattice dimension *via* a strategic compositional engineering, generally a doping of the anion or cation sites. Hence, we believe that the development of new active species of this kind by employing different ion doping strategies is a rational choice to attempt the improvement of $A_3B_2X_9$-type materials based photovoltaic performances.

Another strategy to promote progresses in this direction is through the improvement of the quality of the thin films based on these species. Bismuth halides based compounds crystallize directly and

rapidly into a textured polycrystalline microstructure. New preparation methods need to be developed or more widely implemented to exert a tight control on the crystallization process, for example those like the two-steps solution processing, thermal evaporation, dip-coating and vapor assisted solution processing methods, to cite a few. All of these deposition methods have been shown to hold the potential to form denser films compared to the traditional one-step solution processing.

Rudorffite structures are considered competitive candidates to perovskites ~~derivatives~~ for the realization of well-performing photovoltaic devices. However, as an excess of defects introduced during thin films processing makes the photoelectric performance weak, they still hold difficulties to compete with the classical perovskite structures.

As for the case of the double perovskites, we can state that the large, indirect bandgaps of the currently fabricated Ag-Bismuth halides based materials are the cause of their limited photovoltaic performance. The alloying/doping can help in reducing the optical band gap. The synthesized $Cs_2TlBiBr_6$ compound has a similar energy bands structure to that of lead-based perovskites, but its application is limited by the high toxicity of Tl. A new double perovskite of formula $FA_4GeSbCl_{12}$ has a smaller bandgap of 1.3 eV. Hence, it is necessary to further explore other double perovskite structures or to apply complex compositional engineering strategies in the search for species with energy bands structures similar to those of lead-based materials. This field is undoubtedly very challenging and wide open to new exciting discoveries.

Generally, research on group VA-based lead-free perovskites and their derivatives have reached good achievements in some aspects, but mechanisms of films formation, charge separation and recombination at interfaces and grain boundaries need to be studied more deeply, especially for gaining more information on the defects nature, in comparison with the lead-based counterparts, for which scientists have reached nowadays a high level of understanding of these aspects. Therefore, further research should focus on developing new group VA metals-based materials with suitable bandgaps and benign defects characteristics. At the same time, the investigation of novel film fabrication strategies need to be boosted, to obtain high quality light absorbing films and to improve the quality of the interfaces with the charge extracting ancillary layers (ETL and HTL). We believe that, if these investigations will be systematically implemented, a fast and significant improvement of the photovoltaic performances will be achieved employing the new group VA metals-based perovskites and their derivatives in light harvesting systems.

Conflicts of interest

There are no conflicts to declare.

Acknowledgements

This work was supported by the National Natural Science Foundation of China (NSFC) (No. 61775091, 21671160, 51761145048, 21833009), Natural Science Foundation of Shenzhen Innovation Committee (Nos. JCYJ20180504165851864) and the Shenzhen Key Laboratory Project (No. ZDSYS201602261933302). T. G. acknowledges the DFG support via the GRK (Research Training Group) 2204 "Substitute Materials for Sustainable Energy Technologies".

References

1 https://www.nrel.gov/pv/assets/pdfs/best-research-cell-efficiencies.20191106.pdf).
2 G. E. Eperon, S. D. Stranks, C. Menelaou, M. B. Johnston, L. M. Herz and H. J. Snaith, *Energy Environ. Sci.*, 2014, **7**, 982-988.
3 M. M. Lee, J. Teuscher, T. Miyasaka, T. N. Murakami and H. J. Snaith, *Science*, 2012, **338**, 643.
4 S. D. Stranks, G. E. Eperon, G. Grancini, C. Menelaou, M. J. P. Alcocer, T. Leijtens, L. M. Herz, A. Petrozza and H. J. Snaith, *Science*, 2013, **342**, 341.
5 W.-J. Yin, T. Shi and Y. Yan, *Adv. Mater.*, 2014, **26**, 4653-4658.
6 G. Giorgi, J.-I. Fujisawa, H. Segawa and K. Yamashita, *J. Phys. Chem. C*, 2014, **118**, 12176-12183.
7 J. You, Z. Hong, Y. Yang, Q. Chen, M. Cai, T.-B. Song, C.-C. Chen, S. Lu, Y. Liu, H. Zhou and Y. Yang, *ACS Nano*, 2014, **8**, 1674-1680.

Please do not adjust margins

8 F. Hao, C. C. Stoumpos, P. Guo, N. Zhou, T. J. Marks, R. P. H. Chang and M. G. Kanatzidis, *J. Am. Chem. Soc.*, 2015, **137**, 11445-11452.
9 P.-P. Sun, Q.-S. Li, L.-N. Yang and Z.-S. Li, *Nanoscale*, 2016, **8**, 1503-1512.
10 B. Saparov, F. Hong, J.-P. Sun, H.-S. Duan, W. Meng, S. Cameron, I. G. Hill, Y. Yan and D. B. Mitzi, *Chem. Mater.*, 2015, **27**, 5622-5632.
11 B.-W. Park, B. Philippe, X. Zhang, H. Rensmo, G. Boschloo and E. M. J. Johansson, *Adv. Mater.*, 2015, **27**, 6806-6813.
12 W. Zhang, Y. Sui, B. Kou, Y. Peng, Z. Wu and J. Luo, *ACS Appl. Mater. Interfaces*, 2020, **12**, 9141-9149.
13 D. Cortecchia, H. A. Dewi, J. Yin, A. Bruno, S. Chen, T. Baikie, P. P. Boix, M. Grätzel, S. Mhaisalkar, C. Soci and N. Mathews, *Inorg. Chem.*, 2016, **55**, 1044-1052.
14 A. Zakutayev, C. M. Caskey, A. N. Fioretti, D. S. Ginley, J. Vidal, V. Stevanovic, E. Tea and S. Lany, *J. Phys. Chem. Lett.*, 2014, **5**, 1117-1125.
15 C. Wu, Q. Zhang, G. Liu, Z. Zhang, D. Wang, B. Qu, Z. Chen and L. Xiao, *Adv. Energy Mater.*, 2020, **10**, 1902496.
16 A. J. Lehner, D. H. Fabini, H. A. Evans, C.-A. Hébert, S. R. Smock, J. Hu, H. Wang, J. W. Zwanziger, M. L. Chabinyc and R. Seshadri, *Chem. Mater.*, 2015, **27**, 7137-7148.
17 S.-Y. Kim, Y. Yun, S. Shin, J. H. Lee, Y.-W. Heo and S. Lee, *Scripta Mater.*, 2019, **166**, 107-111.
18 R. L. Z. Hoye, R. E. Brandt, A. Osherov, V. Stevanović, S. D. Stranks, M. W. B. Wilson, H. Kim, A. J. Akey, J. D. Perkins, R. C. Kurchin, J. R. Poindexter, E. N. Wang, M. G. Bawendi, V. Bulović and T. Buonassisi, *Chem. – Eur. J.*, 2016, **22**, 2605-2610.
19 M. Vigneshwaran, T. Ohta, S. Iikubo, G. Kapil, T. S. Ripolles, Y. Ogomi, T. Ma, S. S. Pandey, Q. Shen, T. Toyoda, K. Yoshino, T. Minemoto and S. Hayase, *Chem. Mater.*, 2016, **28**, 6436-6440.
20 L. Liang and P. Gao, *Adv. Sci.*, 2018, **5**, 1700331.
21 D. M. Fabian and S. Ardo, *J. Mater. Chem. A*, 2016, **4**, 6837-6841.
22 H. Dammak, A. Yangui, S. Triki, Y. Abid and H. Feki, *J. Lumin.* 2015, **161**, 214-220.
23 T. Li, Y. Hu, C. A. Morrison, W. Wu, H. Han and N. Robertson, *Sustain. Energy Fuels*, 2017, **1**, 308-316.
24 S. Sun, S. Tominaka, J.-H. Lee, F. Xie, P. D. Bristowe and A. K. Cheetham, *APL Mater.*, 2016, **4**, 031101.
25 G. Giorgi and K. Yamashita, *Chem. Lett.*, 2015, **44**, 826-828.
26 A. H. Slavney, T. Hu, A. M. Lindenberg and H. I. Karunadasa, *J. Am. Chem. Soc.*, 2016, **138**, 2138-2141.
27 E. T. McClure, M. R. Ball, W. Windl and P. M. Woodward, *Chem. Mater.*, 2016, **28**, 1348-1354.
28 I. Turkevych, S. Kazaoui, E. Ito, T. Urano, K. Yamada, H. Tomiyasu, H. Yamagishi, M. Kondo and S. Aramaki, *ChemSusChem*, 2017, **10**, 3754-3759.
29 J.-P. Correa-Baena, L. Nienhaus, R. C. Kurchin, S. S. Shin, S. Wieghold, N. T. Putri Hartono, M. Layurova, N. D. Klein, J. R. Poindexter, A. Polizzotti, S. Sun, M. G. Bawendi and T. Buonassisi, *Chem. Mater.*, 2018, **30**, 3734-3742.
30 J. Pal, S. Manna, A. Mondal, S. Das, K. V. Adarsh and A. Nag, *Angew. Chem. Int. Edit.*, 2017, **56**, 14187-14191.
31 J. Zaleski, R. Jakubas, L. Sobczyk and J. Mróz, *Ferroelectrics*, 1990, **103**, 83-90.
32 J.-C. Hebig, I. Kühn, J. Flohre and T. Kirchartz, *ACS Energy Lett.*, 2016, **1**, 309-314.
33 A. Karmakar, M. S. Dodd, S. Agnihotri, E. Ravera and V. K. Michaelis, *Chem. Mater.*, 2018, **30**, 8280-8290.
34 G. Tang, Z. Xiao, H. Hosono, T. Kamiya, D. Fang and J. Hong, *J. Phys. Chem. Lett.*, 2018, **9**, 43-48.
35 B. Vargas, R. Torres-Cadena, J. Rodríguez-Hernández, M. Gembicky, H. Xie, J. Jiménez-Mier, Y.-S. Liu, E. Menéndez-Proupin, K. R. Dunbar, N. Lopez, P. Olalde-Velasco and D. Solis-Ibarra, *Chem. Mater.*, 2018, **30**, 5315-5321.
36 M. Pham, J. Harris, J. Shaffer, A. Daniel, S. Chowdhury, A. Ali, S. Banerjee and S. Ahmed, *J. Mater. Sci. - Mater. El.*, 2019, **30**, 9438-9443.
37 M. Righetto, D. Meggiolaro, A. Rizzo, R. Sorrentino, Z. He, G. Meneghesso, T. C. Sum, T. Gatti and F. Lamberti, *Prog. Mater. Sci.*, 2020, **110**, 100639.
38 D. Meggiolaro and F. De Angelis, *ACS Energy Lett.*, 2018, **3**, 2206-2222.
39 F. Giustino and H. J. Snaith, *ACS Energy Lett.*, 2016, **1**, 1233-1240.
40 G. Volonakis, M. R. Filip, A. A. Haghighirad, N. Sakai, B. Wenger, H. J. Snaith and F. Giustino, *J. Phys. Chem. Lett.*, 2016, **7**, 1254-1259.
41 X.-G. Zhao, J.-H. Yang, Y. Fu, D. Yang, Q. Xu, L. Yu, S.-H. Wei and L. Zhang, *J. Am. Chem. Soc.*, 2017, **139**, 2630-2638.
42 C. N. Savory, A. Walsh and D. O. Scanlon, *ACS Energy Lett.*, 2016, **1**, 949-955.
43 Z. Chu, T. Siohwa, G. Liguo, K. Yusuke and M. A. Tingli, Proc. SPIE 2018.
44 I. Benabdallah, M. Boujnah, A. El Kenz, A. Benyoussef, M. Abatal and A. Bassam, *J. Alloy. Comp.*, 2019, **773**, 796-801.
45 Y.-Y. Sun, J. Shi, J. Lian, W. Gao, M. L. Agiorgousis, P. Zhang and S. Zhang, *Nanoscale*, 2016, **8**, 6284-6289.
46 M. Kumar Chini, S. Goverapet Srinivasan, N. K. Tailor, Yukta, D. Salahub and S. Satapathi, *Chem. Phys.*, 2020, **529**, 110547.
47 X.-G. Zhao, D. Yang, J.-C. Ren, Y. Sun, Z. Xiao and L. Zhang, *Joule*, 2018, **2**, 1662-1673.
48 G. Volonakis, A. A. Haghighirad, H. J. Snaith and F. Giustino, *J. Phys. Chem. Lett.*, 2017, **8**, 3917-3924.
49 J. Yang, P. Zhang and S.-H. Wei, *J. Phys. Chem. Lett.*, 2018, **9**, 31-35.
50 Z. Xiao, Y. Yan, H. Hosono and T. Kamiya, *J. Phys. Chem. Lett.*, 2018, **9**, 258-262.
51 W. Deng, Z.-Y. Deng, J. He, M. Wang, Z.-X. Chen, S.-H. Wei and H.-J. Feng, *Appl. Phys. Lett.*, 2017, **111**, 151602.
52 R. X. Yang, K. T. Butler and A. Walsh, *J. Phys. Chem. Lett.*, 2015, **6**, 5009-5014.

Formattato: Italiano (Italia)
Formattato: Tedesco (Germania)
Formattato: Tedesco (Germania)
Formattato: Italiano (Italia)
Formattato: Tedesco (Germania)
Formattato: Tedesco (Germania)
Formattato: Tedesco (Germania)
Formattato: Tedesco (Germania)

53 S. Öz, J.-C. Hebig, E. Jung, T. Singh, A. Lepcha, S. Olthof, F. Jan, Y. Gao, R. German, P. H. M. van Loosdrecht, K. Meerholz, T. Kirchartz and S. Mathur, *Sol. Energy Mater. Sol. C.*, 2016, **158**, 195-201.

54 M. Lyu, J.-H. Yun, M. Cai, Y. Jiao, P. V. Bernhardt, M. Zhang, Q. Wang, A. Du, H. Wang, G. Liu and L. Wang, *Nano Res.*, 2016, **9**, 692-702.

55 X. Zhang, G. Wu, Z. Gu, B. Guo, W. Liu, S. Yang, T. Ye, C. Chen, W. Tu and H. Chen, *Nano Res.*, 2016, **9**, 2921-2930.

56 T. Singh, A. Kulkarni, M. Ikegami and T. Miyasaka, *ACS Appl. Mater. Interfaces*, 2016, **8**, 14542-14547.

57 M. Abulikemu, S. Ould-Chikh, X. Miao, E. Alarousu, B. Murali, G. O. Ngongang Ndjawa, J. Barbé, A. El Labban, A. Amassian and S. Del Gobbo, *J. Mater. Chem. A*, 2016, **4**, 12504-12515.

58 M.-C. Tang, D. Barrit, R. Munir, R. Li, J. M. Barbé, D.-M. Smilgies, S. Del Gobbo, T. D. Anthopoulos and A. Amassian, *Solar RRL*, 2019, **3**, 1800305.

59 Z. Zhang, X. Li, X. Xia, Z. Wang, Z. Huang, B. Lei and Y. Gao, *J. Phys. Chem. Lett.*, 2017, **8**, 4300-4307.

60 S. M. Jain, D. Phuyal, M. L. Davies, M. Li, B. Philippe, C. De Castro, Z. Qiu, J. Kim, T. Watson, W. C. Tsoi, O. Karis, H. Rensmo, G. Boschloo, T. Edvinsson and J. R. Durrant, *Nano Energy*, 2018, **49**, 614-624.

61 C. Ran, Z. Wu, J. Xi, F. Yuan, H. Dong, T. Lei, X. He and X. Hou, *J. Phys. Chem. Lett.*, 2017, **8**, 394-400.

62 A. Kulkarni, T. Singh, M. Ikegami and T. Miyasaka, *RSC Adv.*, 2017, **7**, 9456-9460.

63 S. S. Mali, H. Kim, D.-H. Kim and C. Kook Hong, *ChemistrySelect*, 2017, **2**, 1578-1585.

64 F. Lamberti, T. Gatti, E. Cescon, R. Sorrentino, A. Rizzo, E. Menna, G. Meneghesso, M. Meneghetti, A. Petrozza and L. Franco, *Chem*, 2019, **5**, 1806-1817.

65 S. S. Shin, J. P. Correa Baena, R. C. Kurchin, A. Polizzotti, J. J. Yoo, S. Wieghold, M. G. Bawendi and T. Buonassisi, *Chem. Mater.*, 2018, **30**, 336-343.

66 H. Li, C. Wu, Y. Yan, B. Chi, J. Pu, J. Li and S. Priya, *ChemSusChem*, 2017, **10**, 3994-3998.

67 T. Okano and Y. Suzuki, *Mater. Lett.*, 2017, **191**, 77-79.

68 J. Huang, Z. Gu, X. Zhang, G. Wu and H. Chen, *J. Alloy. Comp.*, 2018, **767**, 870-876.

69 C. Lan, J. Luo, S. Zhao, C. Zhang, W. Liu, S. Hayase and T. Ma, *J. Alloy. Comp.*, 2017, **701**, 834-840.

70 H. Wang, J. Tian, K. Jiang, Y. Zhang, H. Fan, J. Huang, L.-m. Yang, B. Guan and Y. Song, *RSC Adv.*, 2017, **7**, 43826-43830.

71 M. Chen, L. Wan, M. Kong, H. Hu, Y. Gan, J. Wang, F. Chen, Z. Guo, D. Eder and S. Wang, *J. Alloy. Comp.*, 2018, **738**, 422-431.

72 F. Li, H. Fan, P. Wang, X. Li, Y. Song and K.-J. Jiang, *J. Mater. Sci.*, 2019, **54**, 10371-10378.

73 F. Bai, Y. Hu, Y. Hu, T. Qiu, X. Miao and S. Zhang, *Sol. Energy Mater. Sol. C.*, 2018, **184**, 15-21.

74 M. B. Johansson, H. Zhu and E. M. J. Johansson, *J. Phys. Chem. Lett.*, 2016, **7**, 3467-3471.

75 H. Zhu, M. B. Johansson and E. M. J. Johansson, *ChemSusChem*, 2018, **11**, 1114-1120.

76 D. B. Khadka, Y. Shirai, M. Yanagida and K. Miyano, *J. Mater. Chem. C*, 2019, **7**, 8335-8343.

77 K. K. Bass, L. Estergreen, C. N. Savory, J. Buckeridge, D. O. Scanlon, P. I. Djurovich, S. E. Bradforth, M. E. Thompson and B. C. Melot, *Inorg. Chem.*, 2017, **56**, 42-45.

78 M. Leng, Z. Chen, Y. Yang, Z. Li, K. Zeng, K. Li, G. Niu, Y. He, Q. Zhou and J. Tang, *Angew. Chem. Int. Edit.*, 2016, **55**, 15012-15016.

79 Y. Shen, J. Yin, B. Cai, Z. Wang, Y. Dong, X. Xu and H. Zeng, *Nanoscale Horiz.*, 2020, **5**, 580-585.

80 M.-Q. Li, Y.-Q. Hu, L.-Y. Bi, H.-L. Zhang, Y. Wang and Y.-Z. Zheng, *Chem. Mater.*, 2017, **29**, 5463-5467.

81 S. F. Hoefler, T. Rath, R. Fischer, C. Latal, D. Hippler, A. Koliogiorgos, I. Galanakis, A. Bruno, A. Fian, T. Dimopoulos and G. Trimmel, *Inorg. Chem.*, 2018, **57**, 10576-10586.

82 S. Zhang, R. Xu, Z. Li, Q. Zhang, L. Cheng, Z. Wang and C. Fu, *J. Adv. Dielec.*, 2019, **09**, 1950013.

83 J. Li, X. Liu, J. Xu, J. Chen, C. Zhao, M. Salma Maneno, B. Zhang and J. Yao, *Solar RRL*, 2019, **3**, 1900218.

84 B.-B. Yu, M. Liao, J. Yang, W. Chen, Y. Zhu, X. Zhang, T. Duan, W. Yao, S.-H. Wei and Z. He, *J. Mater. Chem. A*, 2019, **7**, 8818-8825.

85 A. Maiti, G. Paul, H. Bhunia and A. J. Pal, *Sol. Energy Mater. Sol. C.*, 2019, **200**, 109941.

86 Y.-Q. Hu, H.-Y. Hui, W.-Q. Lin, H.-Q. Wen, D.-S. Yang and G.-D. Feng, *Inorg. Chem.*, 2019, **58**, 16346-16353.

87 X.-L. Li, L.-L. Gao, B. Ding, Q.-Q. Chu, Z. Li and G.-J. Yang, *J. Mater. Chem. A*, 2019, **7**, 15722-15730.

88 C. Wu, Q. Zhang, Y. Liu, W. Luo, X. Guo, Z. Huang, H. Ting, W. Sun, X. Zhong, S. Wei, S. Wang, Z. Chen and L. Xiao, *Adv. Sci.* 2018, **5**, 1700759.

89 E. Greul, Michiel L. Petrus, A. Binek, P. Docampo and T. Bein, *J. Mater. Chem. A*, 2017, **5**, 19972-19981.

90 W. Ning, F. Wang, B. Wu, J. Lu, Z. Yan, X. Liu, Y. Tao, J.-M. Liu, W. Huang, M. Fahlman, L. Hultman, T. C. Sum and F. Gao, *Adv. Mater.*, 2018, **30**, 1706246.

91 M. Pantaler, K. T. Cho, V. I. E. Queloz, I. García Benito, C. Fettkenhauer, I. Anusca, M. K. Nazeeruddin, D. C. Lupascu and G. Grancini, *ACS Energy Lett.*, 2018, **3**, 1781-1786.

92 M. Wang, P. Zeng, S. Bai, J. Gu, F. Li, Z. Yang and M. Liu, *Solar RRL*, 2018, **2**, 1800217.

93 W. Gao, C. Ran, J. Xi, B. Jiao, W. Zhang, M. Wu, X. Hou and Z. Wu, *ChemPhysChem*, 2018, **19**, 1696-1700.

94 X. Yang, Y. Chen, P. Liu, H. Xiang, W. Wang, R. Ran, W. Zhou and Z. Shao, *Adv. Funct. Mater.*, 2020, **30**, 2001557.

95 C. Zhang, L. Gao, S. Teo, Z. Guo, Z. Xu, S. Zhao and T. Ma, *Sustain. Energy Fuels*, 2018, **2**, 2419-2428.

96 A. H. Slavney, L. Leppert, D. Bartesaghi, A. Gold-Parker, M. F. Toney, T. J. Savenije, J. B. Neaton and H. I. Karunadasa, *J. Am. Chem. Soc.*, 2017, **139**, 5015-5018.

97 Y. Liu, L. Zhang, M. Wang, Y. Zhong, M. Huang, Y. Long and H. Zhu, *Mater. Today*, 2019, **28**, 25-30.

98 Z. Deng, F. Wei, S. Sun, G. Kieslich, A. K. Cheetham and P. D. Bristowe, *J. Mater. Chem. A*, 2016, **4**, 12025-12029.

Formattato: Tedesco (Germania)

Formattato: Tedesco (Germania)

Formattato: Italiano (Italia)

Formattato: Tedesco (Germania)

99 F. Wei, Z. Deng, S. Sun, F. Zhang, D. M. Evans, G. Kieslich, S. Tominaka, M. A. Carpenter, J. Zhang, P. D. Bristowe and A. K. Cheetham, *Chem. Mater.*, 2017, **29**, 1089-1094.

100 T. T. Tran, J. R. Panella, J. R. Chamorro, J. R. Morey and T. M. McQueen, *Mater. Horiz.*, 2017, **4**, 688-693.

101 J. Xiu, Y. Shao, L. Chen, Y. Feng, J. Dai, X. Zhang, Y. Lin, Y. Zhu, Z. Wu, Y. Zheng, H. Pan, C. Liu, X. Shi, X. Cheng and Z. He, *Mater. Today Energy*, 2019, **12**, 186-197.

102 A. K. Baranwal, H. Masutani, H. Sugita, H. Kanda, S. Kanaya, N. Shibayama, Y. Sanehira, M. Ikegami, Y. Numata, K. Yamada, T. Miyasaka, T. Umeyama, H. Imahori and S. Ito, *Nano Converg.*, 2017, **4**, 26.

103 K. M. Boopathi, P. Karuppuswamy, A. Singh, C. Hanmandlu, L. Lin, S. A. Abbas, C. C. Chang, P. C. Wang, G. Li and C. W. Chu, *J. Mater. Chem. A*, 2017, **5**, 20843-20850.

104 A. Singh, K. M. Boopathi, A. Mohapatra, Y. F. Chen, G. Li and C. W. Chu, *ACS Appl. Mater. Interfaces*, 2018, **10**, 2566-2573.

105 F. Jiang, D. Yang, Y. Jiang, T. Liu, X. Zhao, Y. Ming, B. Luo, F. Qin, J. Fan, H. Han, L. Zhang and Y. Zhou, *J. Am. Chem. Soc.*, 2018, **140**, 1019-1027.

106 F. Umar, J. Zhang, Z. Jin, I. Muhammad, X. Yang, H. Deng, K. Jahangeer, Q. Hu, H. Song and J. Tang, *Adv. Opt. Mater.*, 2019, **7**, 1801368.

107 P. C. Harikesh, H. K. Mulmudi, B. Ghosh, T. W. Goh, Y. T. Teng, K. Thirumal, M. Lockrey, K. Weber, T. M. Koh, S. Li, S. Mhaisalkar and N. Mathews, *Chem. Mater.*, 2016, **28**, 7496-7504.

108 S. Weber, T. Rath, K. Fellner, R. Fischer, R. Resel, B. Kunert, T. Dimopoulos, A. Steinegger and G. Trimmel, *ACS Appl. Energy Mater.*, 2019, **2**, 539-547.

109 K. Ahmad, P. Kumar and S. M. Mobin, *ChemElectroChem*, 2020, **7**, 946-950.

110 P. Karuppuswamy, K. M. Boopathi, A. Mohapatra, H.-C. Chen, K.-T. Wong, P.-C. Wang and C.-W. Chu, *Nano Energy*, 2018, **45**, 330-336.

111 Y. Yang, C. Liu, M. Cai, Y. Liao, Y. Ding, S. Ma, X. Liu, M. Guli, S. Dai and M. K. Nazeeruddin, *ACS Appl. Mater. Interfaces*, 2020, **12**, 17062-17069.

112 S. Chatterjee and A. J. Pal, *ACS Appl. Mater. Interfaces*, 2018, **10**, 35194-35205.

113 T. Li, X. Wang, Y. Yan and D. B. Mitzi, *J. Physi. Chem. Lett.*, 2018, **9**, 3829-3833.

114 R. Nie, A. Mehta, B.-w. Park, H.-W. Kwon, J. Im and S. I. Seok, *J. Am. Chem. Soc.*, 2018, **140**, 872-875.

115 C. Zuo and L. Ding, *Angew. Chem. Int. Edit.*, 2017, **56**, 6528-6532.

116 B. Vargas, E. Ramos, E. Pérez-Gutiérrez, J. C. Alonso and D. Solis-Ibarra, *J. Am. Chem. Soc.*, 2017, **139**, 9116-9119.

117 W. B. Dai, S. Xu, J. Zhou, J. Hu, K. Huang and M. Xu, *Sol. Energy Mater. Sol. C.*, 2019, **192**, 140-146.

118 Z. Shao, T. Le Mercier, M. B. Madec and T. Pauporté, *Mater. Design*, 2018, **141**, 81-87.

119 Y. Kim, Z. Yang, A. Jain, O. Voznyy, G.-H. Kim, M. Liu, L. N. Quan, F. P. García de Arquer, R. Comin, J. Z. Fan and E. H. Sargent, *Angew. Chem. Int. Edit.*, 2016, **55**, 9586-9590.

120 H. C. Sansom, G. F. S. Whitehead, M. S. Dyer, M. Zanella, T. D. Manning, M. J. Pitcher, T. J. Whittles, V. R. Dhanak, J. Alaria, J. B. Claridge and M. J. Rosseinsky, *Chem. Mater.*, 2017, **29**, 1538-1549.

121 N. Pai, J. Lu, T. R. Gengenbach, A. Seeber, A. S. R. Chesman, L. Jiang, D. C. Senevirathna, P. C. Andrews, U. Bach, Y.-B. Cheng and A. N. Simonov, *Adv. Energy Mater.*, 2019, **9**, 1803396.

122 B. Ghosh, B. Wu, X. Guo, P. C. Harikesh, R. A. John, T. Baikie, Arramel, A. T. S. Wee, C. Guet, T. C. Sum, S. Mhaisalkar and N. Mathews, *Adv. Energy Mater.*, 2018, **8**, 1802051.

123 Z. Hu, Z. Wang, G. Kapil, T. Ma, S. Iikubo, T. Minemoto, K. Yoshino, T. Toyoda, Q. Shen and S. Hayase, *ChemSusChem*, 2018, **11**, 2930-2935.

124 B. Zhang, Y. Lei, R. Qi, H. Yu, X. Yang, T. Cai and Z. Zheng, *Sci. China Mater.*, 2019, **62**, 519-526.

Formattato: Tedesco (Germania)

Formattato: Tedesco (Germania)